The Meteoritical Society

Meteoritics & Planetary Science 50, Nr 4, 604–631 (2015)
doi: 10.1111/maps.12393

Highly siderophile element (HSE) abundances in the mantle of Mars are due to core formation at high pressure and temperature

K. RIGHTER[1*], L. R. DANIELSON[2], K. M. PANDO[2], J. WILLIAMS[3], M. HUMAYUN[3], R. L. HERVIG[4], and T. G. SHARP[4]

[1]Mailcode KT, NASA Johnson Space Center, 2101 NASA Parkway, Houston, Texas 77058, USA
[2]Jacobs Technology, JETS, NASA Johnson Space Center, 2101 NASA Parkway, Houston, Texas 77058, USA
[3]National High Magnetic Field Laboratory and Department of Earth, Ocean and Atmospheric Science, Florida State University, Tallahassee, Florida 32310–3706, USA
[4]ASU School of Earth and Space Exploration, PO Box 871404, Tempe, Arizona 5287–1404, USA
[*]Corresponding author. E-mail: kevin.righter-1@nasa.gov

(Received 10 February 2014; revision accepted 07 October 2014)

Abstract–Highly siderophile elements (HSEs) can be used to understand accretion and core formation in differentiated bodies, due to their strong affinity for FeNi metal and sulfides. Coupling experimental studies of metal–silicate partitioning with analyses of HSE contents of Martian meteorites can thus offer important constraints on the early history of Mars. Here, we report new metal–silicate partitioning data for the PGEs and Au and Re across a wide range of pressure and temperature space, with three series designed to complement existing experimental data sets for HSE. The first series examines temperature effects for D (HSE) in two metallic liquid compositions—C-bearing and C-free. The second series examines temperature effects for D(Re) in FeO-bearing silicate melts and FeNi-rich alloys. The third series presents the first systematic study of high pressure and temperature effects for D(Au). We then combine our data with previously published partitioning data to derive predictive expressions for metal–silicate partitioning of the HSE, which are subsequently used to calculate HSE concentrations of the Martian mantle during continuous accretion of Mars. Our results show that at midmantle depths in an early magma ocean (equivalent to approximately 14 GPa, 2100 °C), the HSE contents of the silicate fraction are similar to those observed in the Martian meteorite suite. This is in concert with previous studies on moderately siderophile elements. We then consider model calculations that examine the role of melting, fractional crystallization, and sulfide saturation/undersaturation in establishing the range of HSE contents in Martian meteorites derived from melting of the postcore formation mantle. The core formation modeling indicates that the HSE contents can be established by metal–silicate equilibrium early in the history of Mars, thus obviating the need for a late veneer for HSE, and by extension volatile siderophile elements, or volatiles in general.

INTRODUCTION

Siderophile element concentrations in planetary mantles can be estimated using simple models for melting, and element correlations (e.g., Drake 1980). For example, reconstruction of the mantle concentrations of moderately siderophile elements (MSE—Ni, Co, Mo, and W) in asteroid 4 Vesta (from HED meteorites) led to production of a model that is in excellent agreement with subsequent spacecraft measurements (e.g., Righter and Drake 1997a, 1997b; Russell et al. 2012). Similar calculations have been done for MSE in the Moon and Mars over several decades (e.g., Newsom 1984; Treiman et al. 1987; Righter 2002; Righter and Chabot 2011), and have placed constraints on the differentiation history of both of these bodies as well.

The highly siderophile elements (Au, Re, and the platinum group elements, PGE) can provide constraints

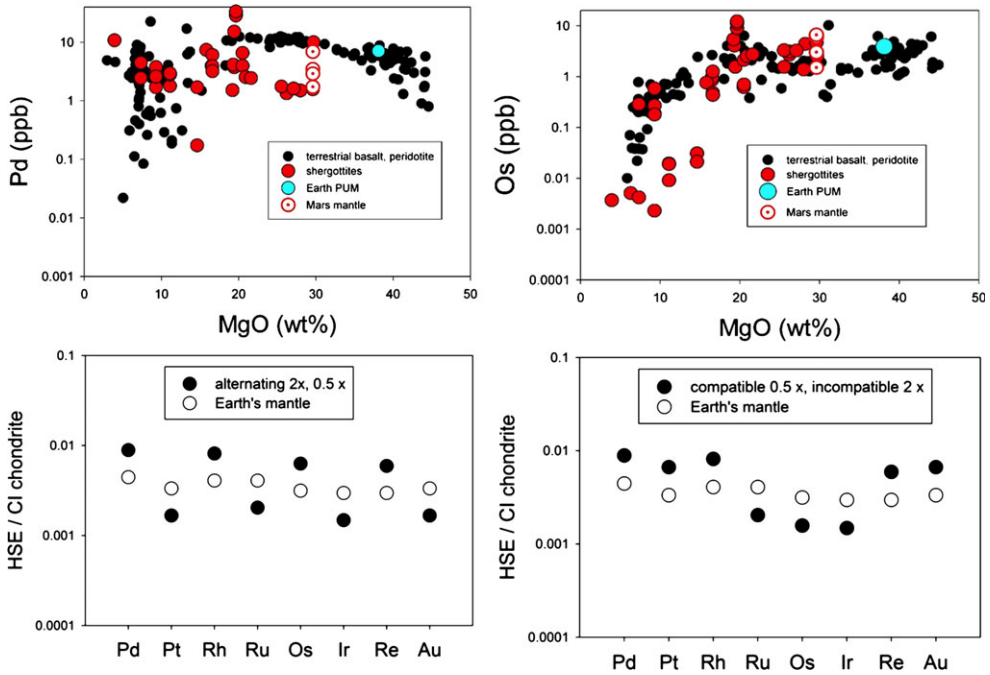

Fig. 1. HSE in Mars (A: Os-MgO and B: Pd-MgO diagram) showing overlap between terrestrial and Martian magmas. Also shown are hypothetical 2*x* and 0.5*x* chondritic HSE values as plotted in (C) and (D). These values fall within the broad array of data for the Os-MgO and Pd-MgO plots, and illustrate that significant deviations from chondritic will not be obvious on plots using log scale across several orders of magnitude HSE concentration. Data sources: Terrestrial samples: Gueddari et al. (1996), Lorand et al. (1999, 2000), Meisel et al. (2001), Schmidt et al. (2000), Handler and Bennett (1999), Crocket et al. (1997), Rehkämper et al. (1999), Vogel and Keays (1997), Brügmann et al. (1987), Puchtel and Humayun (2000, 2005), and Puchtel et al. (2009). Martian meteorites: Dreibus et al. (2000), Shirai and Ebihara (2004), McSween and Jarosewich (1983), Taylor et al. (2002), Neal et al. (2001), Barrat et al. (2002), Sarbadhikari et al. (2009), Zipfel et al. (2000), Anand et al. (2008), Smith et al. (1984), Ma et al. (1982), Dreibus et al. (1982), Burgess et al. (1989), Warren et al. (1996), Walker et al. (2002), Puchtel et al. (2008), Jones et al. (2003), Walker et al. (2009), Burghele et al. (1983), Brandon et al. (2012), Filiberto et al. (2012), Riches et al. (2011), and Yang et al. (2014).

on the processes of core formation and accretion for differentiated bodies (Shirey and Walker 1998). Core formation is the most important fractionation mechanism for the HSE, because metal concentrates HSE by several orders of magnitude over the silicate, leaving very low concentrations of HSE in the mantle. On the other hand, high concentrations and near-chondritic relative ratios of HSEs in the terrestrial upper mantle have been used to argue for the addition of chondritic material to the Earth's upper mantle following core formation (Kimura et al. 1974; Chou 1978). High and similar HSE contents between Martian meteorites and terrestrial mantle and basalt samples have led many researchers to suggest that the Martian mantle accreted chondritic material after the formation of its large metallic core (e.g., Kong et al. 1999; Warren et al. 1999; Walker 2009; Bottke et al. 2010; Brandon et al. 2012) (Fig. 1). Also, the HSEs Os, Pt, and Re, as part of the Re-Os and Pt-Os isotopic systems, have been used to argue for multiple and ancient mantle reservoirs within the Martian mantle (Brandon et al. 2000; Walker et al. 2008a). However, 2*x* to 3*x* deviations from chondritic values on an HSE-MgO diagram may not be detectable in such large areas of the plot—for any given MgO content there is a 3 order of magnitude variation in HSE content (Fig. 1), indicating that use of these diagrams does not provide compelling arguments for a chondritic mantle, and alternatives to late veneer explanations should be sought.

In particular, detailed HSE modeling during core formation has not been attempted for Mars, for various reasons. HSE partitioning between metal and silicate melt has been notoriously difficult to study, plagued by analytical barriers (low concentrations at natural doping levels) and experimental issues (e.g., the nugget effect). However, new studies have emerged that seem to be free of these problems (e.g., Righter et al. 2008a; Brenan and McDonough 2009; Mann et al. 2012), allowing modeling to be carried out more confidently. Nonetheless, even a recent attempt to model HSEs in Mars completely ignores the large and well-known effect of S (Rai and Van Westrenen 2013), and relies

only on one S-free experimental study carried out under a narrow range of conditions (Mann et al. 2012), despite the well-known S-rich nature of Mars (Clark and Baird 1979; Dreibus and Wänke 1985; Burns 1987).

To evaluate whether the HSE content of the Martian mantle truly requires influx of material by late accretion, or can be explained by core formation, we have undertaken new experiments to help constrain the metal–silicate partitioning behavior of the HSE. Combining these results with previously published studies, we derive predictive expressions for D(met/sil) for the HSE. Modeling core formation utilizing the PT conditions derived from the moderately and slightly siderophile elements (Righter and Chabot 2011; Yang et al. 2014) allows the HSE content of the primitive Martian mantle to be calculated. Then, variations of HSE in Martian mantle melts are examined by modeling mantle melting, fractional crystallization, and sulfide saturation, for comparison to Martian meteorite samples. It will be shown that the Martian meteorite HSE abundances can be explained by derivation from a primitive mantle with a nonchondritic HSE pattern, thus obviating the need for late chondritic accretion to Mars.

NEW EXPERIMENTAL DATA

Three series of experiments were undertaken to address aspects of HSE partitioning between metal and silicate melt. Because solubilities of HSE are very low in silicate melts, measurements can be best made on large glass or silicate samples. High pressure experiments are typically very small <1 mm, and studies of systematic behavior of HSE in metal–silicate systems can be difficult due to the size requirements for analysis. For that reason, and because there are few systematic studies across temperature, we have carried out experiments at fixed pressure—near 1 GPa—and variable temperatures. Because of the paucity of data on Re partitioning between metallic liquids and silicate melts, we designed the first series of experiments to focus on understanding Re partitioning at low to intermediate pressures. The second series included all eight HSEs so that elements could be compared directly at any given set of conditions. The third series focused on Au at variable pressure. Little to no systematic data for Au as a function of pressure have been published, whereas there exist several studies of Au at 1 bar and variable temperatures. Of all three series, only the Au-series found significant micronuggets in the silicate melt, and that issue was addressed using a combined approach of ion probe and TEM analysis (see the Au Experiments [0.9–23 GPa] section).

Re Experiments (1–1.6 GPa)

Experiments were done in a 13 mm piston cylinder apparatus; basalt samples were held in FeNiCo alloy capsules. We prepared a synthetic basalt in the system SiO_2-Al_2O_3-FeO-MgO-CaO, mixed from high-purity oxides, and doped with several wt% of ReO_2. The Re alloyed with the FeNiCo and left only ppm levels in the silicate melt. Run products include mostly silicate melt (quenched to a glass) with minor pyroxenes, garnet (Fig. 2), or FeNiCoRe alloy (Righter and Hauri 1998). Barium carbonate pressure media were used in the piston cylinder assemblies, and temperature was imposed by graphite heaters and controlled with a type C (W_3Re-$W_{26}Re$) thermocouple (Righter et al. 1997). fO_2 is calculated from the activities of Fe and FeO in the metal and glass phases, respectively (see Righter et al. 1997). Oxygen fugacities (fO_2) in these experiments are approximately 0–1 log fO_2 units below the iron-wüstite (IW) buffer. Samples were pressurized to the desired run pressure plus 15% (some readjustment of pressure to the desired value was necessary), and then heated at a rate of approximately 40 °C min^{-1}. After being held at the set point temperature for 24–48 h, the power to the furnace was turned off, which caused quench of the sample usually dropping to 100 °C within 10–15 s of powering off. Typical run products of equilibrated glass and metal are shown in Fig. 2A.

Major elements in the crystals and glasses from the experimental run products (Table 1) were analyzed with a CAMECA SX50 electron microprobe at The University of Arizona. Operating conditions for analysis of major elements in crystals and glasses were 15 kV accelerating voltage, 30 nA sample current, 10 s counting times, and a point beam; PAP ϕ-ρ-z correction procedures were used (Pouchou and Pichoir 1991). Standards used include diopside (Si, Mg, and Ca), fayalite (Fe), and potassium feldspar (Al). Analysis of run products for Re was done using SIMS on a CAMECA 6f-series ion probe at the Department of Terrestrial Magnetism, Washington, DC, as outlined by Righter and Hauri (1998).

HSE Experiments (1 GPa)

All experiments were performed using a 13 mm non-end-loaded piston cylinder apparatus (Quickpress, Depths of the Earth Company) at constant pressure using $BaCO_3$ pressure medium. Two different types of capsules were used: MgO and graphite. The sample used for these experiments was a powder containing 70 wt% Knippa basalt composition described in Lewis et al. (1993), and 30 wt% Fe_{60}-HSE_{40} (wt%) metal

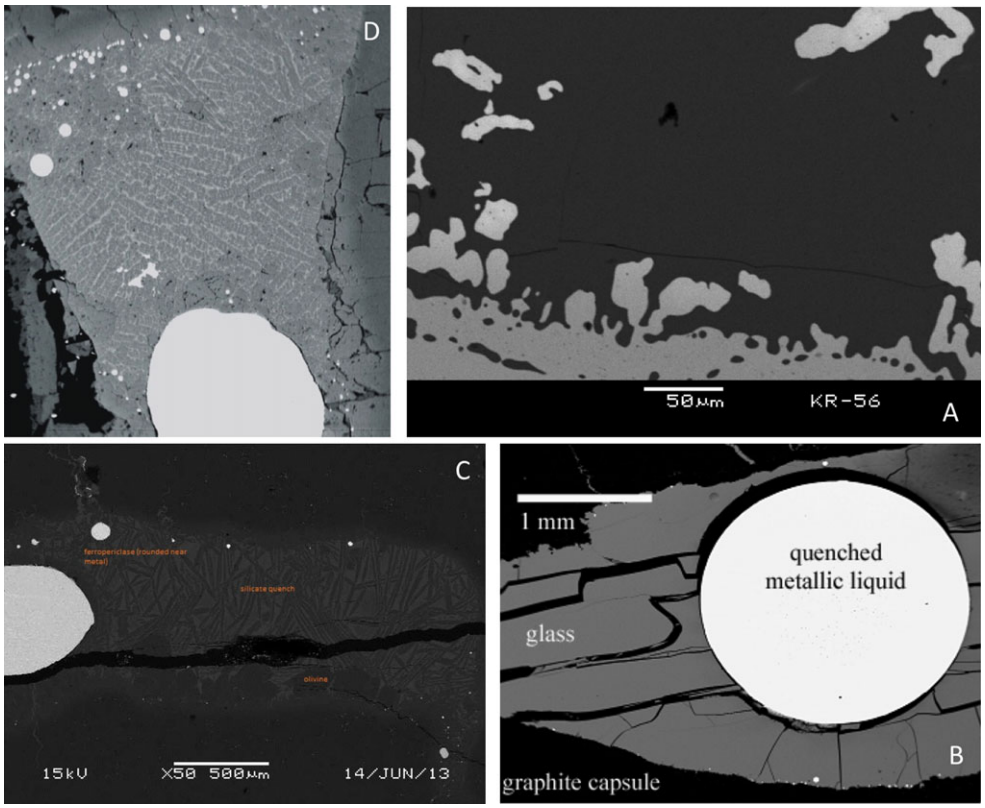

Fig. 2. A) Backscattered electron (BSE) images of a Re-series experiment (KR-56), which shows metal and glass. B) BSE image of an HSE-series experiment using a C capsule (expt. HSEqp-5). C) BSE image of an HSE-series run using an MgO capsule (expt. HSEqp-10). D) BSE image of run products from Au-series experiment BB175. Sulfide quench products form large round blebs in the bottom of MgO capsules; smaller blebs adhere to the capsule walls. The silicate fraction contains crystalline quench phases of olivine, with interstitial pyroxene and magnesiowüstite.

mixture, where HSEs included Au, Re, and the PGE. Once the samples were brought to a constant pressure of 1.0 GPa, they were then heated to the target temperature. Samples were brought to temperatures high enough to attain equilibrium, based on previous experiments using similar materials and elements (Righter et al. 1997, 2010, 2011). The temperature was measured using type C thermocouple (W-Re) wires with an accuracy of ±2 °C. Samples were quenched by turning off the power and adjusting oil pressure to maintain isobaric conditions, until the temperature reached 100 °C. The HSE-series consisted of experiments in both MgO and C capsules between 1500 °C and 1900 °C (Figs. 2B and 2C; Table 2).

The graphite capsules reacted with the metallic portion of the starting material to form C-bearing metallic liquids. The measured C contents in the quenched metallic liquids were between 3.5 and 4.5 wt%, which corresponds to X_C (mole fraction of C in Fe metal) = 0.21 (±0.01), in agreement with previous studies of Fe-C alloys in this pressure range (Dasgupta and Walker 2008; Righter et al. 2010). For the Fe-C system, between temperatures of 1300 °C and 1800 °C, the carbon solubility curve is nearly vertical at roughly 5.5 wt% C in the Fe metal. In the Fe-C-HSE system, the amount of C will be lower than in the Fe-C binary (simply by dilution effects of the HSEs), but the metallic liquid C content is nearly constant over this temperature range. Therefore, for the graphite capsule experiments, the silicate and metallic melt compositions are nearly constant over the span of temperatures in this study.

There were significant differences in silicate melt MgO (wt%) with increasing temperature for the experiments that were run in MgO capsules (Table 2). The starting material originally contained approximately 13% MgO, but as the basalt reacted with the capsules, the amount of MgO within the sample increased to between 20 and 40 wt% (also seen by Righter et al. 2010, 2011). The range of melt compositions in this series spans relatively polymerized basalt to depolymerized peridotite. One way of characterizing the degree of silicate melt depolymerization is to calculate the NBO/T value, which is the ratio of nonbridging

Table 1. Experimental conditions and results for Re-series (parenthetical numbers indicate error for the analyses; number in parentheses is associated with last digits of value).

Sample	KR-40	KR-45	KR-47	KR-53	KR-55	KR-56
P (GPa)	1.5	1.0	1.55	1.6	1.5	1.5
T (°C)	1300	1300	1300	1400	1350	1450
Duration (hours)	6.7	24	24	19.5	23.5	3
Silicate						
SiO_2 (wt%)	41.9 (8)	47.2 (9)	45.3 (9)	44.3 42.93	43.2 (9)	42.9 (9)
Al_2O_3	11.79 (24)	13.17 (26)	11.6 (2)	11.39 (23)	9.4 (2)	11.1 (2)
FeO	30.4 (6)	24.74 (49)	28.50 (57)	27.93 (56)	32.8 (7)	30.0 (6)
MgO	4.73 (9)	3.27 (7)	3.70 (7)	5.29 (11)	3.0 (1)	5.2 (1)
CaO	9.36 (19)	10.37 (21)	9.29 (19)	9.67 (19)	9.68 (19)	9.37 (19)
Total	98.14	98.68	98.39	98.58	98.06	98.65
Re (ppm)	1.65 (17)	6.9 (7)	1.2 (1)	4.0 (4)	4.7 (5)	1.4 (2)
Metal						
Fe (wt%)	46.2 (9)	44.7 (9)	42.7 (9)	40.4 (8)	40.9 (8)	43.6 (9)
Ni	28.1 (6)	22.2 (4)	24.2 (5)	20.6 (4)	22.0 (4)	27.8 (6)
Co	15.5 (3)	16.3 (3)	13.7 (3)	13.0 (3)	13.4 (3)	15.9 (3)
Re	9.3 (2)	15.9 (3)	11.9 (2)	23.7 (5)	21.8 (4)	10.8 (2)
Pd	–	–	5.28 (10)	–	–	–
ΔIW	−0.10	−0.02	−0.23	−0.63	−0.28	−0.70
D (Re)	56400	23000	99200	59250	58900	77140
+	7500	3000	13000	7900	6200	10300
−	6200	2500	11000	6500	5100	8400

oxygens to tetrahedrally coordinated cations as defined by Mysen (1991) and Mills (1993). NBO/T for the silicate melts from MgO capsules ranged up to 4.0, as compared to the melts in graphite capsules, which have a value near 1.4 (Table 2). The combination of experiments using these two capsules thus allows an understanding of melt compositional effects that can be directly applied to understanding metal–silicate partitioning involving peridotite melts.

Each sample was analyzed by an ElectroScientific Instruments (ESI) New Wave UP193FX excimer (193 nm) laser ablation system coupled to a Thermo Element XR inductively coupled plasma mass spectrometer (ICP-MS) at the Plasma Analytical Facility of the National High Magnetic Field Laboratory, Florida State University, for Na_2O, MgO, Al_2O_3, SiO_2, P_2O_5, S, K_2O, CaO, Sc, TiO_2, V, Cr, MnO, FeO_T, Co, Ni, Cu, Zn, Ga, Ge, Mo, Mo, Ru, Rh, Pd, W, Re, Os, Ir, Pt, Au. Relative sensitivity factors were obtained using NIST SRM 610 glass, USGS Basaltic Glasses BHVO-2G, BIR-1G, and BCR-2G for lithophile elements (Jochum et al. 2011), and Hoba IVB (Walker et al. 2008b) and Filomena IIA (Wasson et al. 1989) for siderophile elements (Humayun et al. 2007; Gaboardi and Humayun 2009; Humayun 2012). The metal portions of the samples were measured using a 20 μm raster at 5 μm s^{-1} and 20 Hz, collected with 150 runs. Reported values for each capsule are the average of three analyses for metal and silicate portions. Due to the heterogeneity in the silicate quench because of quench olivine crystals and MgO crystals (from the capsule) scattered throughout, a 50 μm line was scanned at 10 μm s^{-1}, 20 Hz, 100 runs. Single values were examined to screen out spikes associated with MgO crystals. The relative standard deviation (RSD) of HSE abundances in metal from each of the runs was approximately 2%, with the exception of HSEqp-14. The metal in HSEqp-14 did not coalesce into a single homogeneous metallic melt sphere, so analyses were taken on three individual droplets and, therefore, the RSD of HSE abundances in metal of HSEqp-14 averaged 23%. The RSD of HSE abundances in the silicate portions of all capsules averaged approximately 20%.

Au Experiments (0.9–23 GPa)

This series of experiments specifically targeted Au due to the dearth of partitioning data for Au at high pressures and temperatures. A natural chondrite, Richardton H5, was chosen as the starting material to simulate partitioning in the early Earth because (1) its bulk composition is similar to that of the bulk Earth, (2) the sulfur content of the metallic fraction is 12 wt%—in the range of modeled sulfur contents of the Earth's core (8–12 wt%) (Poirier 1994; Holzheid and Grove

Table 2. Experimental conditions and results for HSE-series (1 GPa) (parenthetical numbers indicate precision for the analyses, where number in parentheses is associated with last digits of value).

Sample	HSEqp-14	HSEqp-9	HSEqp-10	HSEqp-13	HSEqp-7	HSEqp-5	HSEqp-4	HSEqp-8	HSEqp-2	HSEqp-3
T (°C)	1500	1600	1700	1900	1500	1600	1700	1800	1800	1900
Capsule	MgO	MgO	MgO	MgO	C	C	C	C	C	C
Duration (min)	180	90	45	10	180	90	45	15	15	10
Silicate										
SiO_2 (wt%)	26.7 (1)	28.35 (60)	30.2 (3)	27.8 (2.9)	38.8 (8)	40.2 (8)	40.4 (8)	39.4 (8)	27.6 (6)	38.4 (8)
TiO_2	5.39 (3)	3.81 (20)	3.28 (3)	2.72 (36)	3.40 (7)	3.30 (7)	3.45 (7)	3.31 (7)	2.38 (5)	3.28 (6)
Al_2O_3	9.69 (1)	9.50 (50)	8.38 (8)	6.91 (83)	13.41 (27)	13.27 (26)	13.00 (26)	13.89 (28)	18.59 (37)	13.42 (27)
FeO	13.20 (1)	10.27 (10)	9.14 (23)	9.73 (25)	13.70 (3)	13.13 (26)	12.51 (25)	13.71 (27)	28.05 (56)	14.60 (30)
MnO	0.182 (1)	0.150 (2)	0.140 (3)	0.110 (10)	0.22 (1)	0.20 (1)	0.19 (1)	0.20 (1)	0.13 (1)	0.20 (1)
MgO	20.7 (2)	30 (2)	33.9 (1)	40.0 (5.6)	14.4 (3)	15.1 (3)	14.3 (3)	13.9 (3)	9.56 (19)	15.2 (3)
CaO	15.64 (9)	12.25 (60)	10.15 (3)	8.73 (1.18)	11.93 (24)	10.48 (21)	11.57 (23)	11.41 (22)	10.58 (21)	11.05 (22)
Na_2O	4.93 (4)	3.27 (20)	2.74 (7)	2.29 (28)	2.49 (5)	2.67 (5)	2.82 (6)	2.58 (5)	1.76 (4)	2.30 (5)
K_2O	2.25 (7)	1.57 (10)	1.34 (3)	1.15 (14)	0.94 (2)	0.98 (2)	1.10 (2)	1.02 (2)	0.69 (1)	0.89 (2)
P_2O_5	1.29 (4)	0.85 (2)	0.68 (1)	0.58 (6)	0.58 (1)	0.58 (1)	0.54 (1)	0.46 (1)	0.50 (1)	0.54 (1)
Total	99.99	99.99	100.00	100.00	99.87	99.89	99.88	99.87	99.84	99.89
Ru (ppm)	0.34 (3)	0.24 (4)	0.32 (5)	0.38 (17)	0.69 (6)	0.05 (1)	0.47 (4)	0.63 (5)	2.0 (2)	2.0 (2)
Rh	0.21 (1)	0.13 (5)	0.25 (5)	0.31 (15)	0.57 (5)	1.28 (10)	0.31 (2)	0.32 (2)	2.0 (2)	1.0 (1)
Pd	0.77 (4)	0.72 (1)	0.89 (11)	1.96 (55)	5.7 (5)	5.34 (43)	8.15 (65)	15.9 (1.3)	26 (2)	25 (2)
Re	0.27 (10)	0.23 (1)	0.23 (7)	0.46 (24)	0.41 (3)	0.13 (1)	0.57 (4)	0.26 (2)	7.0 (6)	1.0 (1)
Os	0.29 (3)	0.27 (7)	0.35 (7)	0.26 (11)	0.71 (6)	0.16 (1)	0.18 (1)	0.27 (2)	1.1 (1)	1.0 (1)
Ir	0.31 (1)	0.22 (4)	0.28 (7)	0.32 (16)	0.74 (6)	0.22 (2)	0.15 (1)	0.40 (3)	1.0 (1)	1.0 (1)
Pt	0.33 (6)	0.18 (5)	0.31 (6)	0.53 (31)	0.92 (7)	0.31 (2)	0.29 (2)	0.60 (5)	7.0 (6)	1.0 (1)
Au	1.43 (7)	2.02 (32)	2.39 (38)	11 (2)	6.2 (5)	16 (1)	34 (3)	91 (7)	136 (11)	150 (12)
Metal										
Fe (wt%)	57 (4)	66.0 (2)	64.0 (2)	61.5 (3)	68.0 (1.4)	71.0 (1.4)	70.0 (1.4)	67.0 (1.3)	52.0 (1.0)	67.0 (1.3)
Ru	4.78 (86)	5.29 (3)	4.37 (13)	4.69 (3)	3.75 (8)	3.72 (7)	3.71 (7)	4.00 (8)	6.17 (12)	4.04 (8)
Rh	3.68 (30)	4.35 (6)	4.48 (11)	4.63 (5)	3.94 (8)	3.81 (8)	4.13 (8)	4.07 (8)	6.63 (13)	4.40 (9)
Pd	8.28 (44)	3.27 (7)	5.98 (16)	6.30 (10)	5.20 (10)	4.88 (9)	5.09 (10)	5.22 (10)	8.52 (17)	5.35 (11)
Re	6.07 (2.83)	4.87 (2)	2.66 (21)	3.13 (1)	2.89 (6)	2.61 (5)	2.69 (5)	3.17 (6)	3.86 (8)	3.10 (6)
Os	3.30 (2.83)	4.05 (2)	2.38 (21)	2.75 (1)	2.25 (5)	2.02 (4)	1.99 (4)	2.35 (5)	2.54 (5)	2.38 (5)
Ir	5.69 (19)	4.99 (4)	3.38 (15)	3.73 (1)	2.77 (6)	2.47 (5)	2.47 (5)	2.93 (6)	3.76 (8)	2.89 (6)
Pt	5.92 (1.17)	4.32 (4)	4.70 (19)	4.91 (1)	4.25 (9)	3.71 (7)	3.70 (7)	4.35 (8)	6.20 (12)	4.29 (8)
Au	5.58 (79)	2.61 (5)	7.79 (6)	8.25 (1)	6.58 (13)	6.11 (12)	6.08 (12)	6.63 (13)	10.02 (20)	6.90 (14)
ΔIW	−1.78	−2.08	−2.25	−2.23	−1.2	−1.18	−1.13	−1.27	−1.3	−0.18
D^{exp} (Ru)	141000	220000	137000	123000	54300	744000	79000	63500	30900	20200
D^{exp} (Rh)	175000	189000	196000	101000	96000	293000	72500	157000	9500	44000
D^{exp} (Pd)	108000	45400	67200	32100	9100	9140	6250	3280	3280	2140
D^{exp} (Re)	225000	212000	116000	68000	70500	201000	47200	122000	5500	31000
D^{exp} (Os)	114000	150000	68000	107000	31700	126000	111000	87000	23000	23800
D^{exp} (Ir)	184000	227000	121000	117000	37400	112000	165000	73300	37600	28900

Table 2. *Continued*. Experimental conditions and results for HSE-series (1 GPa) (parenthetical numbers indicate precision for the analyses, where number in parentheses is associated with last digits of value).

Sample	HSEqp-14	HSEqp-9	HSEqp-10	HSEqp-13	HSEqp-7	HSEqp-5	HSEqp-4	HSEqp-8	HSEqp-2	HSEqp-3
T (°C)	1500	1600	1700	1900	1500	1600	1700	1800	1800	1900
Capsule	MgO	MgO	MgO	MgO	C	C	C	C	C	C
Duration (min)	180	90	45	10	180	90	45	15	15	10
D^{exp} (Pt)	179000	240000	152000	92600	46200	120000	128000	72500	8860	42900
D^{exp} (Au)	39000	18300	55000	57700	46000	42700	42500	46400	70000	48300
D^0 (Ru)	57000	76000	57000	62000	17000	247000	29500	27000	17000	9350
+	+6300	8400	6300	6800	1900	27000	3200	3000	1900	1000
−	−5300	7100	5300	5800	1600	23000	2700	2500	1600	870
D^0 (Rh)	360000	355000	364000	166000	215000	613000	140000	280000	15500	74300
+	39600	39000	40000	18300	23700	67000	15400	31000	1700	8200
−	33500	33000	34000	15400	20000	57000	13000	26000	1400	6900
D^0 (Pd)	29800	13100	20000	12300	1900	2200	1700	1100	1300	770
+	3300	1400	2200	1400	200	240	190	120	140	85
−	2800	1200	1900	1100	180	200	160	100	120	72
D^0 (Re)	91000	72600	48000	34000	21600	67000	17600	52000	3100	14300
+	10000	8000	5300	3700	2400	7400	1900	5700	340	1600
−	8500	6800	4500	3200	2000	6200	1600	4800	290	1300
D^0 (Os)	9200	11400	7400	18000	1800	9300	11000	11000	3800	3600
+	1000	1300	800	2000	200	1000	1200	1200	400	400
−	900	1000	700	1700	170	870	1000	1000	350	330
D^0 (Ir)	15000	17000	13000	20000	2200	8300	16000	9200	6300	4400
+	1700	1900	1400	2200	240	900	1800	1000	700	500
−	1400	1600	1200	1900	200	800	1500	900	600	400
D^0 (Pt)	367000	450000	283000	153000	103000	250000	246000	129000	14500	72400
+	40400	49500	31000	17000	11000	27500	27000	14000	1600	8000
−	34000	41800	26000	14000	9600	23300	22900	12000	1300	6700
D^0 (Au)	10800	5300	16200	22100	9500	10000	11600	15000	28200	17300
+	1200	600	1800	2400	1000	1100	1300	1700	3100	1900
−	1000	500	1500	2100	900	900	1100	1400	2600	1600

Table 3. Experimental conditions and results for Au-series (parenthetical numbers indicate error for the analyses; number in parentheses is associated with last digits of value).

Sample	C2043	H162	BB172	BB175	BB176	BB206	BB209
P (GPa)	3	5	11	13	9	23	21
T (°C)	1750	1750	1700	1750	1800	2368	2494
Duration (m)	5	5	4.3	8.5	6	8	5.5
Silicate							
SiO_2 (wt%)	49.2 (9)	45.7 (9)	40.1 (8)	42.4 (9)	39.9 (8)	50.7 (1.0)	44.3 (9)
Al_2O_3	3.37 (7)	2.87 (6)	2.56 (5)	1.93 (4)	2.25 (5)	2.07 (4)	3.12 (6)
Cr_2O_3	0.71 (1)	0.64 (1)	0.24 (1)	0.29 (1)	0.32 (1)	0.88 (2)	0.42 (1)
FeO	14.0 (3)	15.8 (3)	7.09 (14)	6.62 (13)	7.71 (15)	8.00 (16)	10.8 (2)
MgO	28.1 (5)	30.9 (6)	44.9 (9)	46.2 (9)	46.8 (9)	35.5 (7)	33.6 (7)
CaO	3.04 (6)	3.14 (6)	2.46 (5)	1.94 (4)	2.01 (4)	2.05 (4)	2.04 (4)
Na_2O	–	–	0.95 (2)	0.67 (1)	0.60 (1)	0.75 (2)	0.40 (1)
K_2O	–	–	0.11 (1)	0.050 (1)	0.10 (1)	0.010 (1)	0.060 (1)
P_2O_5	0.030 (1)	0.11 (1)	n.d.	n.d.	0.020 (1)	0.29 (1)	0.12 (1)
Total	98.40	99.23	98.40	100.13	99.62	95.39	99.74
Au (ppm)	1.0 (3)	0.6 (2)	3.71 (10)	3.40 (17)	3.27 (19)	140 (35)	443 (58)
Metal							
Fe (wt%)	78.9 (1.6)	84.1 (1.7)	69.8 (1.4)	79.9 (1.6)	73.4 (1.5)	72.6 (1.5)	59.9 (1.2)
Ni	8.76 (18)	7.41 (15)	7.68 (15)	8.70 (17)	9.99 (2)	10.50 (21)	10.05 (20)
Au	1.23 (2)	1.28 (2)	9.52 (19)	2.82 (6)	4.43 (9)	3.06 (6)	3.16 (6)
S	10.3 (2)	7.14 (14)	12.66 (25)	8.76 (18)	12.75 (26)	12.50 (25)	22.56 (45)
ΔIW	−1.68	−1.64	−2.27	−2.45	−2.22	−2.14	−1.64
D(Au) met/sil	12300	21300	25700	8300	13500	220	71
+/−	+3500	+4800	+1200	+600	+1100	+80	+12
	−2300	−3400	−1200	−550	−1000	−50	−10

2002), and (3) there is abundant material for the experiments. Expecting low levels of Au in the silicate fraction, the starting material was doped with 1.2 wt% Au_2S. Samples quenched to a polycrystalline mass (Fig. 2D). The samples, consisting of silicate and metallic melts during the runs, were contained in single crystal MgO capsules. The MgO capsules minimized run product compositional divergence from the bulk Earth (Table 3).

Experiments above 5 GPa were performed in a Walker-type multianvil apparatus. Pressures from 9 to 13 GPa were obtained using WC cubes with 8 mm truncated-edge lengths (TEL), and those at 19–23 GPa used a 3 mm TEL assembly. Temperatures were 1700–1800 °C (9–13 GPa) and 2250–2500 °C (19–23 GPa) and were approximately 100 °C above the liquidus (Table 3). One advantage of this assembly is the low thermal gradients along the capsule length. We conducted experiments with two thermocouples to test the difference in temperature between the hot spot at the center and the top of the capsule at the normal placement of the thermocouple, and found $\Delta T < 5$ °C at 1600 °C. This result was predicted by experiments of Watson et al. (2002), which suggest that in an 8 mm TEL assembly, the thermal gradient in the central 4 mm of the assembly column should be <25 °C. Thermal profile calculations (Hernlund et al. 2006) also predict this result for this assembly. Experiments below 5 GPa were carried out in an end-loaded piston cylinder apparatus at Australia National University. In contrast to the multianvil experiments, samples were contained in polycrystalline MgO capsules, jacketed by platinum foil. This arrangement also contained both the silicate and sulfide liquids.

Sulfide and ultramafic silicate quench products occur as distinct polycrystalline masses, with a visible fraction of metal-sulfide occurring as micron-sized (or smaller) blebs within the silicate (Fig. 2D). Defocused-beam electron probe analyses of the polyphase quench products gave major element chemistry of the two quenched liquids, including Au in the quenched sulfide liquid. A 50 μm beam at 10 nA (conditions similar to those described by Chabot and Agee 2003) was used on the ASU electron microprobe (JEOL 8600) for silicate analyses and a 30 μm beam was used for sulfide analyses. A smaller beam diameter was chosen for sulfide analyses because of the smaller aerial extent of these domains. At least three analyses were performed in each region and then averaged to give a representative composition for that region.

Au contents of the quenched silicate liquid were obtained using secondary ion mass spectrometry in

depth profiling mode (Hervig et al. 2004). The analyses used a Cameca ims 3f SIMS with a primary beam of K^+ ions and detection of negative secondary ions with 50 ± 20 eV excess kinetic energy. A normal-incidence electron gun was used for charge compensation and the Au signal was calibrated by comparison with NIST SRM glasses 610, 612, and 614 using the analyses of Sylvester and Eggins (1997). Using depth profiles of Au abundance allows the high Au regions (discussed below) to be ignored. The lowest Au signals observed in each depth profile were used in the calculation of the amount of Au in the silicate (Hervig et al. 2004). Au concentrations range from 0.6 ± 0.2 to 443 ± 58 ppmw (ppm by weight). Between three and six depth profiles were averaged for each sample. No systematic variation in amount of Au with distance from the metal-sulfide was observed, suggesting equilibrium was approached.

The depth profiles are interpreted as reflecting contributions from Au in the silicate quench material and from Au-bearing microblebs, or what are more commonly known as "micronuggets." The traditional approach to dealing with "the nugget problem" has been to either conduct experiments under high fO_2 conditions, where microblebs do not form, or to discard analyses that contained anomalously high contributions of the element of interest. Because our experiments were performed at low fO_2 conditions, we encountered numerous microblebs in our analyses. The high depth resolution of our analytical technique allows us to include or exclude contributions from microblebs, depending on their origins.

A Philips CM200-FEG transmission electron microscope (TEM) was used to characterize the silicate quench fraction at the submicrometer scale. Diffraction patterns and energy dispersive spectrometry (EDS) were used to determine the order of crystallization during quench, as well as the crystal structure of these phases. The main goal of the use of TEM, however, was identification and characterization of suspected Au-rich micronuggets in the silicate quench (Fig. 3).

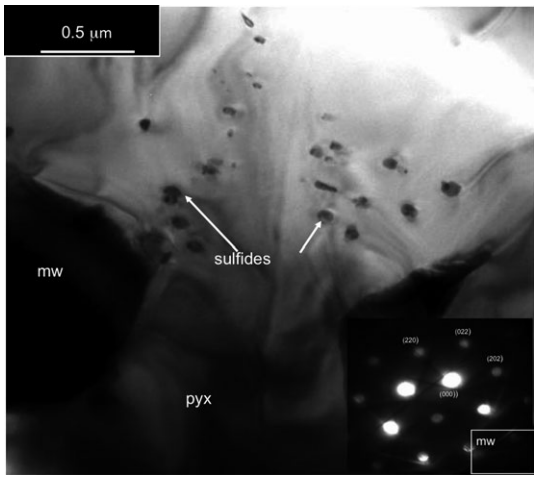

Fig. 3. TEM image, pyx—pyroxene, mw—magnesiowüstite of silicate quench product in Fig. 2D. Convergent beam electron diffraction (CBED) pattern inset is of magnesiowüstite in the image. Submicron sulfides are similar in composition to 100 μm scale sulfide blebs shown in Fig. 2D. These are inferred to be the Au-rich blebs encountered during SIMS analysis of the silicate.

Results (Re, HSE, Au)

Metals from experiments in the HSE-series contained wt% levels of the HSE, far above natural ppm levels found in nature, and must be adjusted to reflect values of the partition coefficient at infinite dilution of the solute. This can be done by recalculating the experimental partition coefficient considering activity coefficients for HSEs in Fe metal. An activity model for multiple HSE-Fe alloys was developed by Mann et al. (2012) that can be used to make this correction to our D(HSE) values by the following relation: $D^{exp} * \gamma_{HSE}/\gamma_{HSE}{}^{0} = D^{0}$ (Mann et al. 2012). Additional simplifying assumptions, above those already made by Mann et al. (2012), are that Au behaves like Pd and Fe-Pd binary data are used for Au-Pd as well, so that the 5-component model can be used. The resulting Ds are tabulated in Table 2. There is no need to correct partition coefficients for the Re-series and Au-series because activity coefficients for Au and Re in Au-Fe and Re-Fe systems are close to unity at the levels of Au and Re in each series (Righter and Drake 1997a, 1997b; Ertel et al. 2001; Liu et al. 2009).

Results for Re show a weak negative temperature dependence of D(Re) metal/silicate between 1500 and 1900 °C, but no trend between 1200 and 1450 °C. The lack of coherent trend is due primarily to small variations in oxygen fugacity and melt composition that produce scatter among D(Re) (Fig. 4A). The combined data from the Au- and HSE-series for D(Au) show a weak temperature effect at <2000 °C, but values much lower at high temperature; the latter could be due to a strong pressure effect (Fig. 4E). The HSE-series exhibits a strong temperature dependence to D(Pd) in both MgO and C capsule results. The graphite capsule experiments yield much lower Ds indicating a large effect of C on D (Pd). For D(Ir), D(Ru), and D(Pt), the C capsule series shows more scatter, masking any temperature effect. The lowest temperature experiment at 1500 °C yielded very low results for Ir and Ru, which may suggest this experiment was compromised by the analyses overlapping on nuggets. D(Pt), D(Ir), and D(Ru) all show weak to no temperature dependence in the MgO

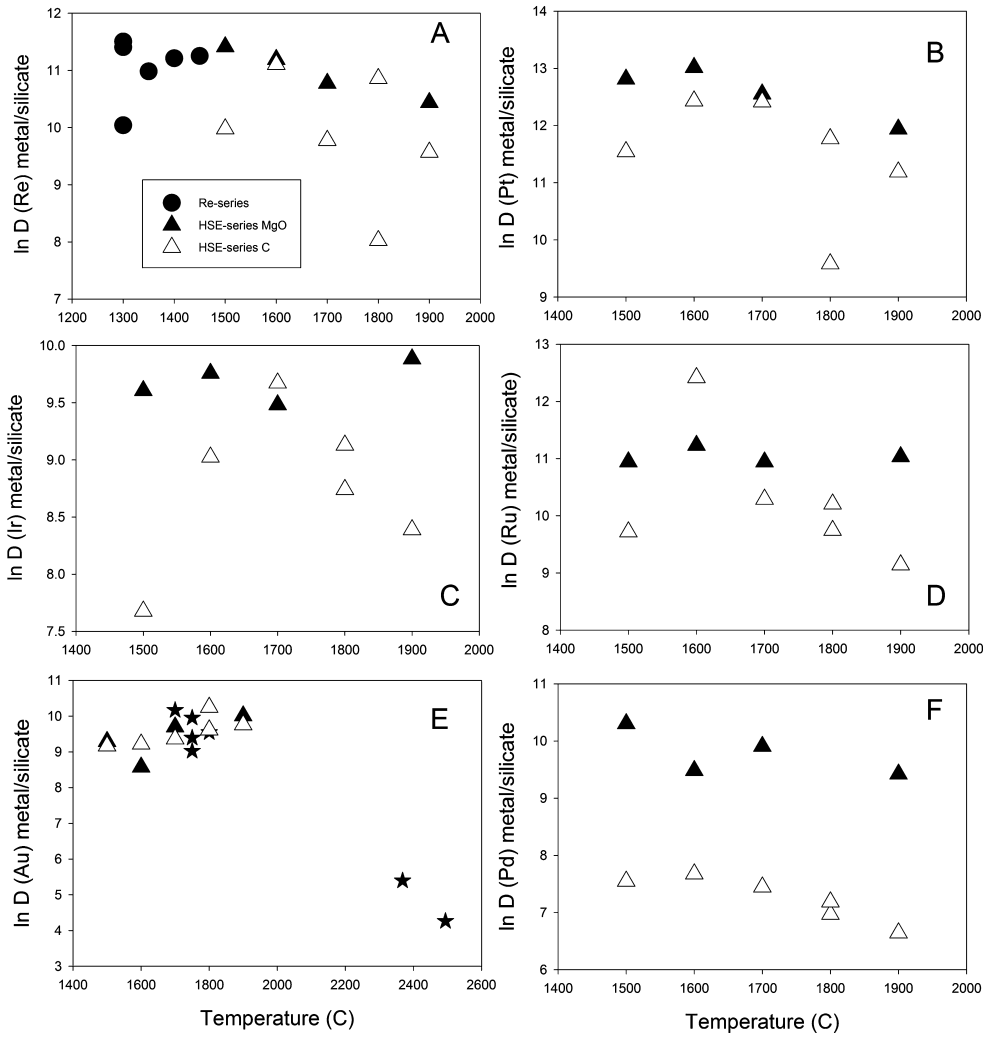

Fig. 4. Results of Re-, HSE-, and Au-series experiments for each element, plotted against temperature. Note the strong temperature dependence of the D(Au) and moderate temperature dependence of the D(Pd) and D(Pt) results compared to the other elements. D(Ru), on the other hand, exhibits little temperature dependence in MgO capsules, but stronger temperature dependence with the graphite capsule experiments. Data from the HSE-series are plotted as the D^0 value, corrected for infinite dilution (see text and Table 2).

capsule experiments and stronger temperature dependence in the C capsules (Figs. 4B, 4C, 4D, and 4F).

PREDICTION OF *D*(METAL/SILICATE) FOR HSE

Metal–silicate partitioning of Re, Au, Pd, Pt, and Ir can be predicted using simple expressions that quantify the dependency on temperature, pressure, oxygen fugacity, and metallic and silicate liquid compositions (Righter 2011; Righter et al. 2011):

$$\ln D = a\ln fO_2 + b/T + cP/T + d(1 - X_S) + e(1 - X_C) + f[\mathrm{NBO/T}] + g \quad (1)$$

where D is the partition coefficient (wt% i in metal/wt% i in silicate); X_S and X_C are the mole fractions of S, C in metallic liquid; and NBO/T is a silicate melt structural parameter that is a proxy for activity of the HSE components in the silicate melt (see the HSE Experiments [1 GPa] section).

Results from the literature are combined to derive the coefficients a to g, and are presented in Table 4 along with uncertainties (Fig. 5). Because the presence of FeO in a silicate melt affects the solubility of HSE (e.g., Laurenz et al. 2010), we have generally omitted studies that utilize FeO-free melts. Regression results yield temperature coefficients that are consistent with the findings of this study in which D(Re), D(Pt), D(Au), and D(Pd) all decrease with increasing temperature,

Table 4. Regression results for D (metal/silicate).

	N	References	a	b	c	d	e	f	g	R^2	2σ
Au	85	[1,2,3,4,5,6]	−0.15 (0.02)	15650 (1500)	31.4 (9.8)	9.0 (0.6)	3.8 (2.3)	−0.21 (0.18)	−0.23 (0.77)	0.821	0.95
Re	51	[1,8,9]	−0.13 (0.21)	−20840 (16300)	24.4 (6.3)	15.0 (5.0)	14.7 (5.1)	−0.77 (0.65)	21.8 (6.2)	0.650	1.20
Ru	32	[1,7,8]	−0.14 (0.11)	−20550 (13900)	2.1 (1.5)	9.4 (4.5)	32.1 (9.6)	−2.6 (1.0)	28.0 (5.7)	0.773	1.14
Pd	135	[1,2,5,7,10,11,12,13,14,15]	−0.15 (0.03)	11800 (2800)	6.8 (2.3)	7.1 (4.1)	15.1 (3.5)	−1.47 (0.23)	5.57 (1.61)	0.804	0.82
Ir	43	[1,3,6,8,16]	−0.05 (0.11)	−17400 (15200)	14.0 (8.0)	17.2 (2.2)	48.0 (5.3)	−3.6 (0.6)	30.8 (5.8)	0.908	1.70
Pt	136	[1,2,7,8,17,18,19,20]	0.15 (0.03)	34300 (3000)	−64.0 (16.0)	15.6 (1.1)	16.0 (4.2)	0.49 (0.30)	−0.42 (2.00)	0.850	1.80

$$\ln D = a\ln fO_2 + b/T + cP/T + d\ln(1 - X_S) + e\ln(1 - X_C) + f(\mathrm{NBO/T}) + g.$$

References: [1] this study; [2] Stone et al. (1990); [3] Crocket et al. (1997); [4] Jones and Drake (1986); [5] Borisov and Palme (1996); [6] Brenan and McDonough (2009); [7] Fleet et al. (1996); [8] Mann et al. (2012); [9] Re-series, this study; [10] Bezmen et al. (1994); [11] Borisov et al. (1994); [12] Righter et al. (2008a, 2008b); [13] Peach et al. (1994); [14] Holzheid et al. (2000); [15] Wheeler et al. (2011); [16] Lindstrom and Jones (1996); [17] Borisov and Palme (1997); [18] Fortenfant et al. (2003); [19] Ertel et al. (2006); [20] Cottrell and Walker (2006).

For Pt, the studies of Stone et al. (1990), Fleet et al. (1996), Borisov and Palme (1997), and Fortenfant et al. (2003) constrain the effect of temperature, fO_2, and S content of the metallic liquid, whereas Cottrell and Walker (2006), Ertel et al. (2006), and Mann et al. (2012) constrain the effects of high pressure and temperature. For Re, the low pressure data of this study constrain the effect of temperature and fO_2, whereas the studies of Mann et al. (2012) constrain the effect of high pressure and temperature; effect of the S content of the metallic liquid is assumed to be the same as for Pt. For Au, the low pressure data of Stone et al. (1990), Crocket et al. (1992), Jones and Drake (1986), and Borisov and Palme (1996) constrain the effect of temperature, fO_2, and S content of the metallic liquid, whereas the studies of Brenan and McDonough (2009) and this study constrain the effect of high pressure and temperature. For Ir, the low pressure data of Crocket et al. (1992) and Lindstrom and Jones (1996) constrain the effect of temperature, fO_2, and S content of the metallic liquid, whereas the study of Brenan and McDonough (2009) constrains the effect of high pressure and temperature. For Pd, the new partitioning data are combined with data used by Righter et al. (2008a, 2008b), which are based on nine studies at various pressure, temperature, fO_2, and metallic liquid compositions.

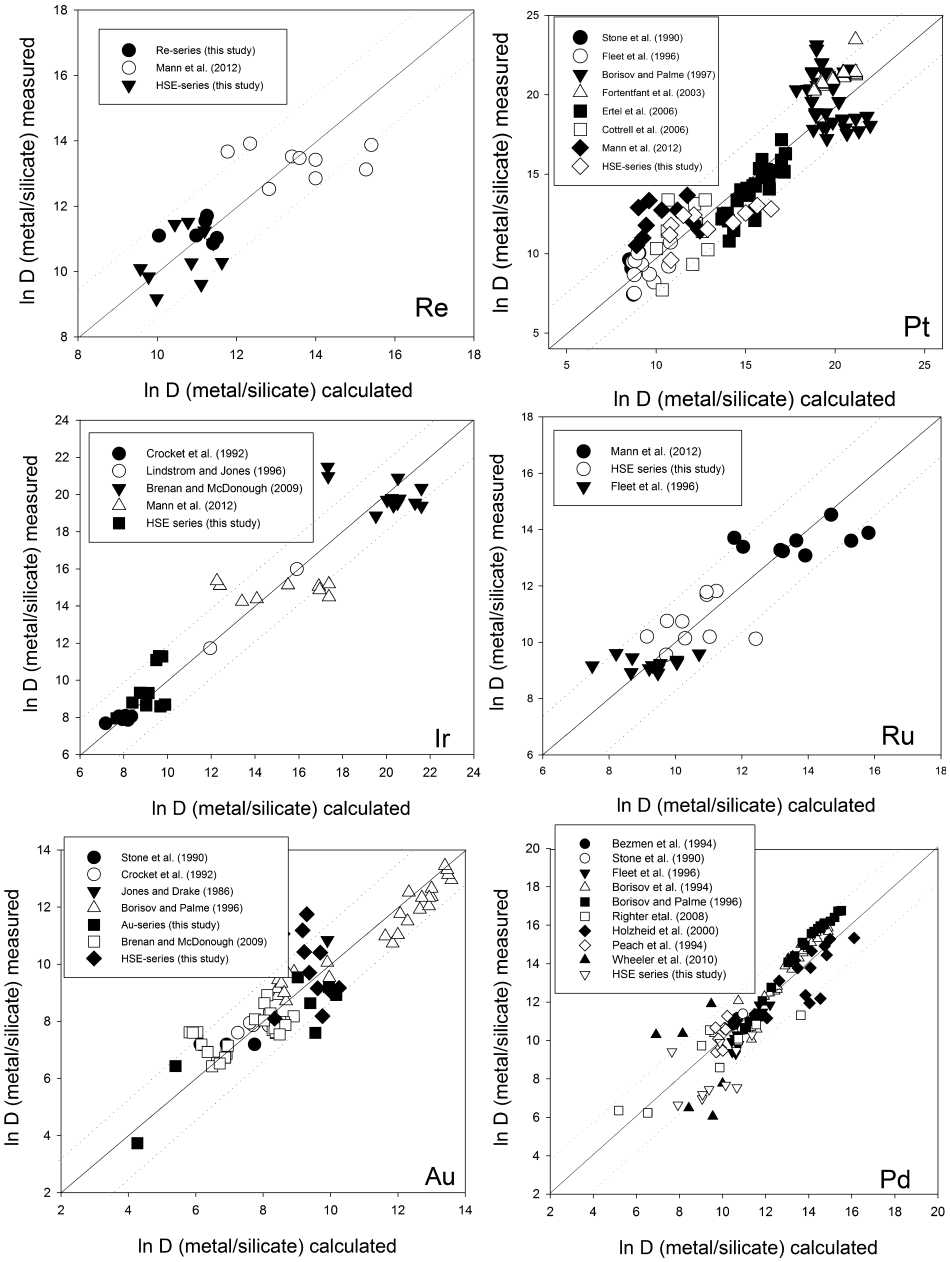

Fig. 5. Results of regression analysis for Re, Pt, Ir, Ru, Au, and Pd metal/silicate experiments from this study as well as data from the literature. Calculated values utilized the expressions and regression coefficients presented in Table 4. Light dashed lines indicate standard error on the regression.

whereas D(Ir) and D(Ru) show less dependence on temperature. Results for the pressure terms are consistent with the small but important pressure dependence measured by Mann et al. (2012) for most HSE. Silicate melt compositional effects are stronger for D(Ru), D(Ir), and D(Pd), and small but still significant for D(Au), D(Re), and D(Pt). The fO_2 terms indicate a 1+ valence for Pt, Pd, and Au, and 2+ for Re dissolved in silicate melt, but a lower valence than generally expected for Ru and Ir (<1+). The effect of S on D(Re) is assumed to be similar to the effect estimated for D (Pt), based on solid metal/liquid metal partitioning results (Chabot et al. 2003; Table 4). Valences lower than expected from 1 bar studies of HSEs have been reported at high PT conditions by others as well (Borisov and Palme 1996; Cottrell and Walker 2006) and for Ir and Ru we have no independent evidence for what the valence should be at high PT conditions.

Finally, the regression coefficients for the S and C contents of the metallic liquid all indicate the presence of these light elements will decrease D(metal/silicate) for all HSEs, as expected from previous studies (e.g., Stone et al. 1990; Fleet et al. 1991, 1996; Crocket et al. 1992; Laurenz et al. 2014). The effect of S is particularly strong for Ir and Pt, and the effect of C is particularly strong for Ru and Ir. Traditional statistical tests such as r^2 (coefficient of determination), t values, P values, and F statistics are used to evaluate and ensure the quality of all the regressions and the significance of each term (a through g; Table 4).

CORE FORMATION MODELING

The abundances of eight siderophile elements (Ni, Co, Mo, W, Ga, P, V, and Cr) in the Martian mantle can be explained by metal–silicate equilibrium during core formation at conditions of 14 GPa and 2000 °C (Righter and Chabot 2011). This PT range is also consistent with lithophile element fractionations established for Sm-Nd, Lu-Hf, Hf-W, and Rb-Sr as measured in Martian meteorites (e.g., Debaille et al. 2008; Mezger et al. 2013). Any modeling of HSE partitioning between core, mantle, and crust must take this first stage of differentiation into account.

The expressions for D(metal/silicate) derived in the Prediction of D(Metal/Silicate) for HSE section can be combined with mass balance equations to calculate the concentration of a siderophile element in the molten portion of the mantle. The distribution of a siderophile element within the solid and liquid (metal and silicate) fractions of a differentiated body is defined by the following mass balance equation (from Righter et al. 1997):

$$C^i_{\text{bulk}} = x\left\{C^i_{\text{LS}}\left[p + (1-p)D^i_{\text{SS/LS}}\right]\right\} + (1-x)\left\{C^i_{\text{LS}}\left[mD^i_{\text{LM/LS}} + \left((1-m)D^i_{\text{SM/LS}}\right)\right]\right\} \quad (2)$$

where x is the fraction of silicate, p is the fraction of molten silicate, m is the fraction of molten metal, C^i_{bulk} is the bulk concentration of siderophile element, C^i_{LS} the concentration of siderophile element in the liquid silicate, $D^i_{\text{SS/LS}}$ is the partition coefficient between solid silicate and liquid silicate, $D^i_{\text{LM/LS}}$ is the partition coefficient between liquid metal and liquid silicate, and $D^i_{\text{SM/LS}}$ is the partition coefficient between solid metal and liquid silicate. In the case of an entirely molten core, $m = 1$, the last term on the right disappears. Rearranging and solving for C^i_{LS} results in:

$$C^i_{\text{LS}} = \frac{C^i_{\text{bulk}}}{x\left[p + (1-p)D^i_{\text{SS/LS}}\right] + (1-x)[mD^i_{LM/LS}]} \quad (3)$$

We consider a simple accretion model in which Mars grows slowly by oligarchic processes, and then more energetic impacts (Senshu et al. 2002; Morishima et al. 2013). If PT evolves along an adiabat, for the Lodders and Fegley (1997) bulk Mars composition, a core mass ($1 - x$) of 21%, a silicate melt fraction (p) of 0.65 (Righter and Chabot 2011), core S and C contents of $X_S = 0.17$ and $X_C = 0.10$, a fixed silicate melt composition of peridotite (or NBO/T = 2.7), and calculated D(metal/silicate) from equation 1, the HSE content of the mantle as Mars grows can be calculated. Recent work shows that 17 siderophile elements (Fe, Ni, Co, Mo, W, Mn, V, Cr, P, Ga, Cu, Sn, Ge, In, Zn, As, and Sb; Righter and Chabot 2011; Yang et al. 2014) in the Martian mantle can be explained as pressure attains approximately 14 GPa, so this is a relevant pressure to examine here. During such an accretion process and at these PT conditions, the calculated HSE mantle abundances (and corresponding D metal/silicate values) are: Au = 0.63 ppb (1000), Pd = 4.22 ppb (600), Pt = 4.98 ppb (900), Re = 0.05 ppb (3200), Ru = 1.8 ppb (1800), Os = 1.8 ppb (1000), and Ir = 2.2 ppb (1000) (Fig. 6; Table 4).

These values can be compared to the HSE contents of shergottites, and for terrestrial basalt and Earth's primitive upper mantle. Because Os exhibits very similar geochemical behavior to Ir, we can use D(Ir) as a proxy for D(Os) and include Os in the application to the Martian mantle as well. It is clear that for the compatible HSE such as Os and Ir, the calculated Os mantle concentration for Mars is within the range for shergottites, and very similar to the range defined by terrestrial basalt and PUM (Figs. 6 and 7). For incompatible HSE, such as Pt, Pd, Au, and Re, the values are typically similar to or slightly lower than those for the terrestrial mantle, and fall along trends with Martian basalts that mimic the trends observed in terrestrial basalt-peridotite suites (Figs. 6 and 7). That is, terrestrial mantle melts typically have higher incompatible HSE contents (especially Au and Pd) than the peridotite or evolved basalts, forming an inverted U-shape pattern. Comparison of the calculated Martian mantle values to the Earth's PUM shows that Pt, Pd, Ir, and Os are similar to Earth (or slightly lower), but the values for Re, Au, and Ru are factors of 7x, 3x, and 5x, respectively, lower than the PUM (Fig. 7). This means that the primitive Martian mantle after core formation would have had broadly chondritic relative HSE contents, but with several elements (Re, Au, and Pd) substantially different than the Earth.

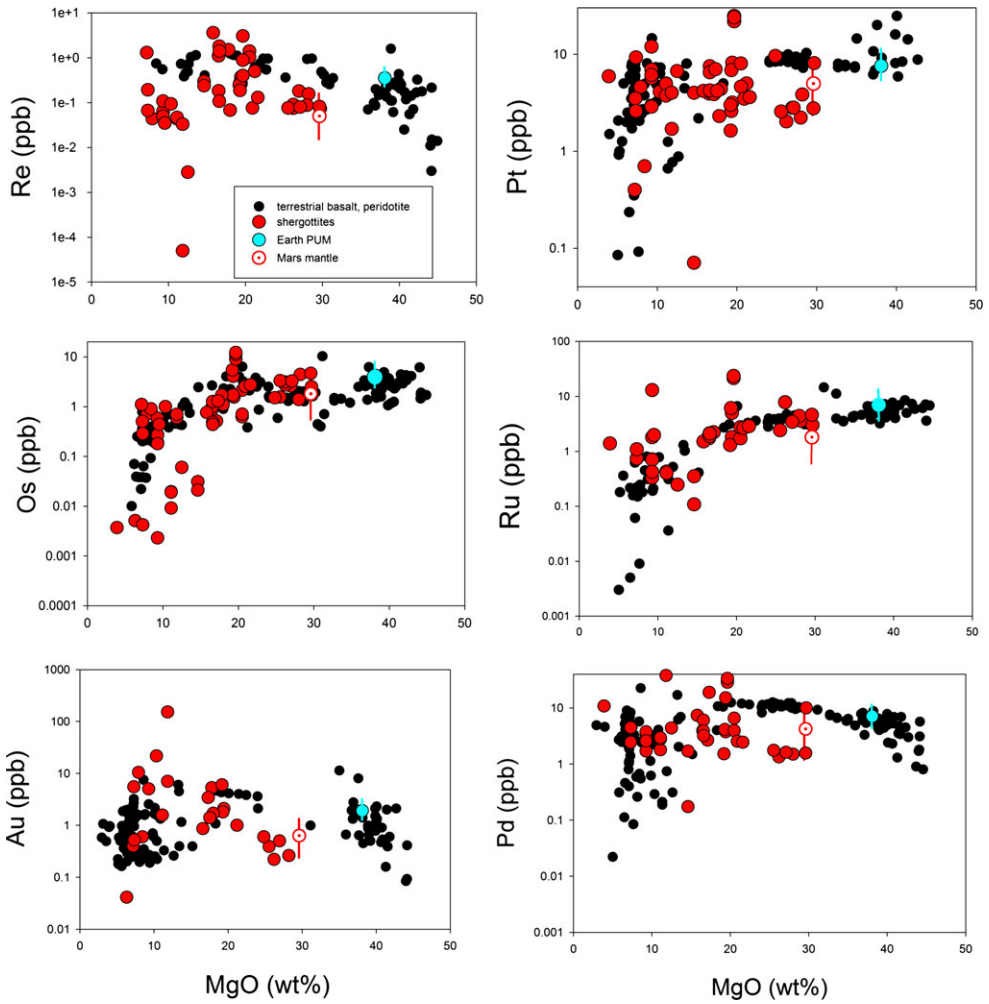

Fig. 6. Variation of HSEs Re, Pt, Ir, Ru, Au, and Pd in olivine-phyric and basaltic shergottites, compared to terrestrial magmas, terrestrial PUM, and the calculated Martian mantle values. The Mars mantle values, for every element, fall near the end of the shergottite array at approximately 30 wt% MgO, indicating that the HSE abundances of the Martian mantle could have been set by core formation and do not require additions from late veneer or late chondritic accretion. The calculated Martian mantle HSE abundances (and corresponding *D* metal/silicate values) are: Au = 0.63 ppb (1000), Pd = 4.22 ppb (600), Pt = 4.98 ppb (900), Re = 0.05 ppb (3200), Ru = 1.8 ppb (1800), Os = 1.8 ppb (1000), and Ir = 2.2 ppb (1000). Data sources same as Fig. 1. Values for bulk HSE content of the Mars are as follows: Re—36 ppb, Os = 400 ppb, Au = 140 ppb, Pd = 560 ppb, Pt = 990 ppb, Ir = 481 ppb, Ru = 790 ppb. *D*(Ir) is used as a proxy for *D*(Os), as discussed in the text.

Subchondritic Re/Os of the primitive Martian mantle may seem counter to evidence from Os isotopes from which suprachondritic sources are suggested, but because Re is incompatible, and Os is compatible during mantle melting, ancient differentiation of Mars probably produced sub- and superchondritic reservoirs that have been mixed over time. For example, Brandon et al. (2000) show that a long-term, Re-depleted source is required for Chassigny, which is consistent with our results. In addition, the work of Brandon et al. (2012) defined a number of samples (Sau 005/008/094, NWA 1195, DaG476, and EET 79001 lithology A, Yamato-980459, and Shergotty) that have subchondritic Re/Os sources (or negative gamma Os values). A subchondritic early primitive mantle and subsequent partitioning between upper and lower mantle (as the mantle may have been only partially molten and not totally molten; Righter and Chabot 2011), and/or cumulate overturn could have produced the enriched and depleted reservoirs that are recognized in isotopic studies (Brandon et al. 2012).

In summary, core formation modeling has shown that the Martian mantle HSE contents can be explained by metal–silicate equilibration at a moderate depth in the Martian mantle—approximately 14 GPa and 2200 K, consistent with many other siderophile elements such as Ni, Co, Mo, W, Cr, and V. During the accretion of Mars, such a depth could have been

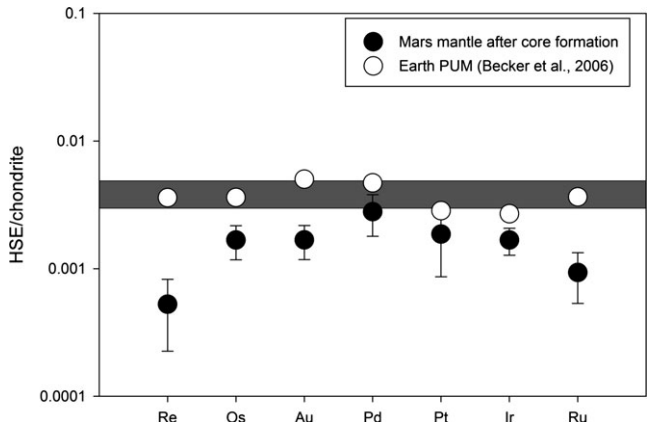

Fig. 7. Calculated Martian mantle HSE concentrations (this study) compared to terrestrial PUM (PUM = Becker et al. 2006; chondritic = CI from compilation of Newsom 1995). The Martian mantle concentrations reflect the HSE content of the mantle after continuous metal–silicate equilibrium has occurred during accretion—by the end of accretion the depth of the magma ocean is 14 (±3 GPa). All HSE are lower than the terrestrial PUM values, but Re and Ru exhibit the largest differences. *D*(Ir) is used as a proxy for *D*(Os), as in Fig. 6.

achieved during a continuous accretion process in which metallic liquid was equilibrating with the molten silicate mantle until the end of accretion where the depth at the bottom of the molten mantle was near 1000 km (Fig. 8). Such a mantle had "broadly chondritic" HSE contents (cf. Walker 2009; Brandon et al. 2012), if such a description allows factors of >2–3*x* chondritic ratios for several elements such as Re, Au, and Ru (Fig. 7).

Late Veneer or Late Accretion Not Required

Late veneer or late chondritic addition has been advocated as an explanation for "broadly chondritic" HSEs in the Martian mantle (Bottke et al. 2010; Brandon et al. 2012; Dale et al. 2012; Rai and Van Westrenen 2013). However, it has been shown in the previous section that core formation can cause "broadly chondritic" (or nonchondritic) HSE ratios in the Martian mantle. There are additional constraints that weaken the idea of late chondritic additions. First, it has been previously suggested that the very low HSE contents of the ancient orthopyroxenite ALH 84001 are evidence that early Mars underwent a core formation event that stripped the mantle of HSE, and then later additions delivered chondritic HSEs (Warren and Kallemeyn 1996; Warren et al. 1999). This has been weakened substantially by new age determinations. Hafnium and Nd isotopic measurements now show that ALH 84001 is much younger—close to 4.0 Ga (Righter et al. 2009a, 2009b; Lapen et al. 2010)—and would not record any pre-late veneer core formation event. Instead, the low HSE concentration in ALH 84001 probably reflects the sulfide saturation of its parental melt, as argued below (see the Fractional Crystallization

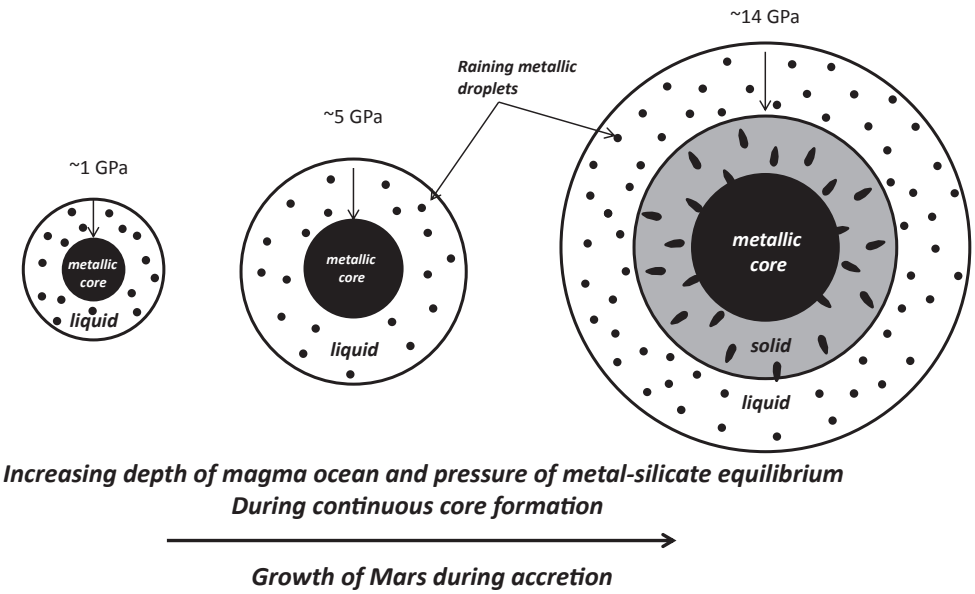

Fig. 8. Schematic illustration of growth of Mars during accretion, in which a magma ocean deepens with time. Metal–silicate equilibrium is continuous as metal is added to the planet and equilibrates with the mantle at the depth of falling/raining droplets allows. As Mars approaches its final size, the depth of the magma ocean is at a pressure of approximately 14 GPa, where many siderophile elements (Fe, Ni, Co, Mo, W, Ga, V, Cr, Mn, Cu, Zn, As, Sb, Sn, In, Ge, and the HSE) can be explained by metal–silicate equilibrium (Righter and Chabot 2011; Yang et al. 2014; this study).

section). Second, the cooling of a Martian magma ocean is going to be rapid, as fast as a few thousand years (e.g., Reese and Solomotov 2006), regardless of the presence of a conducting lid or a thick steam atmosphere. Such crystallization will be so extensive that only a small amount of melt will be left to crystallize deep in the mantle over a few hundred million years. Mixing late chondritic material into this trapped melt is physically implausible, as one cannot expect a vigorously convecting magma ocean once the crystal fraction is over approximately 80% (e.g., Kiefer 2003; Reese and Solomotov 2006). Therefore, the notion that a long duration magma ocean (60–100 Ma; based on Debaille et al. 2008) could allow later chondritic additions to be mixed efficiently into a molten mantle appears untenable as well. The younger ages and longer durations of magma ocean crystallization argued by these previous studies may instead represent the closure ages of the various isotopic systems during cooling of the solid mantle, or even mixing of depleted mantle-derived melts with crustal material (Agee et al. 2013) that is now known to have segregated prior to 4.4 Ga (Humayun et al. 2013). Further, recent work on Martian breccia NWA 7533 shows that chondritic additions were trapped in the thick Martian crust from at least 4428 ± 25 Ma onward forming regolith (Humayun et al. 2013).

HIGHLY SIDEROPHILE ELEMENT CONTENT OF MARTIAN MANTLE AND MELTS

What Causes the Wide Range of HSE in Martian Basaltic Rocks?

If the mantle HSE contents were set by core formation, and yet are similar to the HSE contents of the terrestrial mantle, as suggested by previous studies (i.e., chondritic, near-chondritic, broadly chondritic, or roughly chondritic HSEs; Brandon et al. 2012; Walker 2009), then why do HSE contents of many Martian samples overlap the terrestrial field so extensively and what contributes to the 1000x range of some HSE at a given MgO content? Variability of HSE concentrations within samples has been observed and attributed to a number of factors such as sample mass, nugget effects, terrestrial weathering, shock processes, and contamination during handling (Brandon et al. 2012). We will not review those factors here, but refer the reader to thorough discussions presented in Brandon et al. (2012). Previous studies and reviews have alluded to the importance of fractionation, and sulfide saturation, but these have been superficial treatments that do not incorporate the detailed modeling of major and minor element components (and particularly S concentrations) that is possible with current knowledge. We will focus on the three major issues that affect HSEs: sulfide saturation, mantle melting, and fractional crystallization. We will use mineral/melt partition coefficients for HSE, and S solubility data for Martian melts to examine variation diagrams (HSE-MgO) and the sulfur contents of melts at sulfide saturation (SCSS) to help understand the large variation of HSE contents in Martian meteorites.

Mineral/Melt Partition Coefficients for the HSE

Sulfides

The distribution of HSE in the terrestrial mantle is an important guide to understanding the Martian mantle, and is determined primarily by the stability of metal, sulfide, and/or HSE alloys, all of which have very large partition coefficients (typically >1000) for the HSEs. In particular, the concentrations of HSEs in terrestrial (and Martian) melts are known to be controlled by the presence or absence of sulfide in the residual mantle (e.g., Jagoutz et al. 1979; Mitchell and Keays 1981; Morgan et al. 1981; Barnes et al. 1985; Morgan 1986; Peach et al. 1990; Peach and Mathez 1996; Lorand et al. 2005). In general, large degree partial melts (e.g., komatiites >20–25%) are sulfide undersaturated, the mantle budget of HSEs has been released into the melt (no residual sulfide left in the source; Fig. 9a), and HSE concentrations in the melt are high (e.g., Brügmann et al. 1987; Puchtel et al. 2004; Puchtel and Humayun 2005). Small degree partial melts, such as MORB and OIB, are sulfide-saturated, the mantle budget of the HSE still resides in the residual sulfide (e.g., Morgan and Baedecker 1983; Rehkämper et al. 1999) (Fig. 9a), and HSE concentrations in the melt are low. Secondary fractionation due to crystallization of oxides and silicates can increase the range of values within each kind of rock type. Similar to what is observed in terrestrial basic magmatic suites, Martian basaltic meteorites show a range of values that could be partly explained by sulfide saturation for the lowest values (basaltic shergottites) and sulfide undersaturation for the highest values (olivine-phyric shergottites (Fig. 9B). This will be further evaluated in the Fractional Crystallization section.

Silicates and Oxides

Knowledge of the partitioning behavior of HSE between minerals and melts has increased substantially in the last decade. It is notable that the review of Righter et al. (2000) indicated almost no data for chromite/melt pairs, as well as only preliminary HSE partition coefficients (some for FeO-free systems) for the major silicates—olivine, orthopyroxene, and

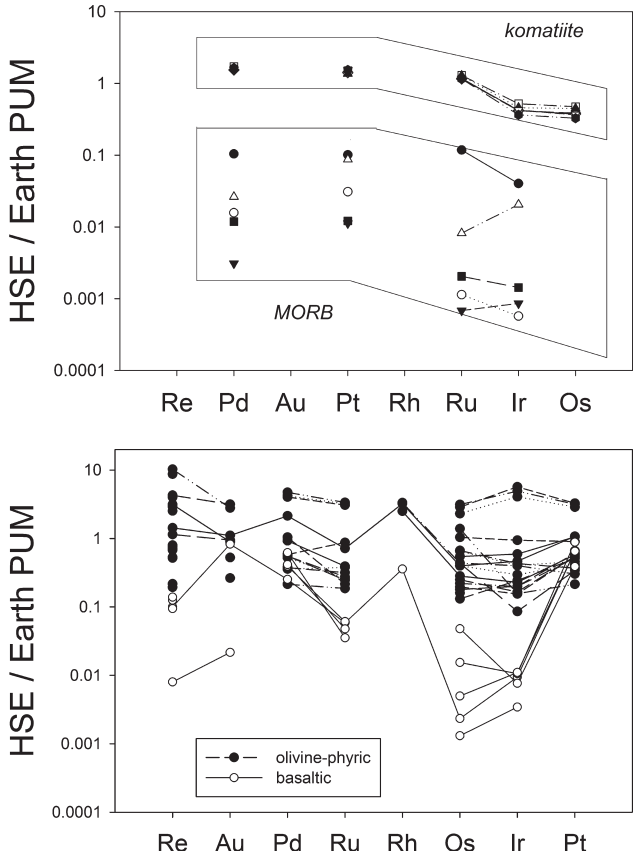

Fig. 9. A) Comparison of HSE contents of MORB (Rehkämper et al. 1999) and komatiite from Munro Township Canada (Puchtel et al. 2004), illustrating the stark difference in HSE content of a sulfide-saturated (MORB) compared to a sulfide-undersaturated (komatiite) melt. B) Selected shergottite HSE concentrations (data sources in Fig. 1) illustrating that the very low HSE contents in some basaltic shergottites may result from sulfide saturation, whereas the higher concentrations in olivine-phyric shergottites result from sulfide undersaturation. All values normalized to Earth PUM values of HSEs from Becker et al. (2006).

clinopyroxene. There have been several pointed studies covering significant territory for the HSE including new data for chromite/melt pairs (Rh, Ru, Os, and Ir; Righter et al. 2004; Brenan et al. 2012); a systematic study of Re (Mallmann and O'Neill 2007); clinopyroxene/melt studies that included three HSEs (Rh and Ru—Hill et al. 2000; Pt—Righter et al. 2004); plagioclase/melt studies that include Au, Pd, and Ru (Sharp et al. 2014); and olivine/melt systems at somewhat oxidized conditions (Ru, Rh—Brenan et al. 2003, 2005). There are still many gaps in our knowledge such as for specific elements (Rh and Ir), or specific phases (orthopyroxene, plagioclase, garnet), but there are enough data to conduct a modeling exercise related to magmatism and mantle evolution for Mars. Partition coefficient values have been chosen for Ir, Os, Ru, Rh, Pt, Pd, Au, and Re, based on these new studies and for the most appropriate compositions or conditions for Martian magmatism (Table 5).

S Contents at Sulfide Saturation

S contents of basaltic melts (SCSS) can be used to determine whether a basalt is S-saturated or S-undersaturated. Experimental studies have demonstrated that the solubility of S in basaltic liquids is a strong function of temperature, pressure, X_{FeO}, and melt composition (e.g., Righter et al. 2009a, 2009b; Ding et al. 2014). For example, basaltic liquids that are FeO-rich, and equilibrated with sulfide at high temperature and low pressure will have the highest S contents. Using the model of Righter et al. (2009a, 2009b), the S content of sulfide-saturated shergottite liquids can be calculated as a function of P and T. The generation of magma in the Martian interior is thought to include a wide range of temperatures, pressures, and melt compositions as well as a restricted range of oxygen fugacities between FMQ-2 and FMQ-3.5 (e.g., Filiberto et al. 2008; Herd 2008; Righter et al. 2008b). Quantification of these parameters with the Righter et al. (2009a, 2009b) expression allows calculation of the S contents as a function of temperature between 1250 and 1550 °C, and pressure up to 1.5 GPa. In this modeling, the results of Rapp et al. (2013) will be emulated where fractionation of a primitive shergottite (such as Yamato-980459) from 1430 °C to more evolved liquids like some basaltic shergottites at 1170 °C, FMQ-3 and 1 bar is modeled, using the MELTS (Ghiorso and Sack 1995) algorithm. Because the effect of oxygen fugacity is very small at these conditions (Fe_2O_3 content is low in this range), it has been fixed at IW+1 for these calculations, based on the most reduced shergottite QUE 94201 (Karner et al. 2007).

The calculations here indicate a narrow and well-defined range of S contents for sulfide-saturated primitive shergottites, and demonstrate that the amount of S in a magma ascending from shallow depth will be between 3000 and 4000 ppm (Fig. 10), whereas at 1.5 GPa it is much lower—close to 1600 ppm. Many olivine-phyric shergottites have as much as 1600 ppm S (Fig. 10A), and although it is tempting to conclude that all olivine-phyric shergottites are sulfide saturated at 1.5 GPa, the data can be interpreted three ways: First, such melts *could* represent SCSS at 1.5 GPa. Because of the negative effect of pressure on SCSS, magmas that rise to the surface at saturation will be undersaturated as they approach the surface and will not regain sulfide saturation until subsequent crystal fractionation to increase the S content. Second, the approximately 1600 ppm could reflect degassing of an ascending, originally SCSS melt. And third, such melts could

Table 5. Experimental mineral/melt partition coefficients (D) for HSE.

Phase/silicate liq.	Re	Pd	Pt	Au	Ru	Os	Ir	References
Sulfide liq. ($\times 10^3$)	0.05–2	1.8–120	0.9–12	2	4.4–46	3.7–430	3.2–200	8–13, 18
	0.3	**5**	**2**	**2**	**8**	**5**	**5**	
Olivine	< 0.01; 0.08[a]	0.12–0.4	<0.009–0.22	0.12	0.2–2.19	>1	0.43–2.7, >7	1, 3, 6, 14, 15, 16, 19
	0.08	**0.1**	**0.01**	**0.12**	**1.0**	**0.8**	**0.8**	
Clinopyroxene	0.035–0.2; 0.8[a]	<0.3	1.4–2.0	0.001–0.1	1–4.27	0.075	–	1, 2, 3, 6, 14, 17
	0.8	**0.05**	**1.5**	**0.05**	**2.0**	**0.3**	**0.3**	
Orthopyroxene	0.013; 0.7[a]	–	–	–	–	–	–	6, 7, 14, 19
	0.7	**0.001**	**0.001**	**0.001**	**0.001**	**0.1**	**0.1**	
Chromite	<0.01	0.14	–	0.1	100–1143	–	230–22000	14, 20
	0.8	**0.1**	**0.001**	**0.1**	**100**	**230**	**230**	
Spinel ($MgAl_2O_4$)	<0.01; 0.8[a]	<0.02	3	0.01	25–28	–	25	1, 3, 4, 5
	0.8	**0.01**	**0.01**	**0.01**	**25**	**25**	**25**	

[1] Malvin et al. (1986); [2] Watson et al. (1987); [3] Capobianco et al. (1991); [4] Capobianco et al. (1994); [5] Capobianco and Drake (1990); [6] Mallmann and O'Neill (2007); [7] Righter and Hauri (1998); [8] Stone et al. (1990); [9] Fleet et al. (1991); [10] Crocket et al. (1992); [11] Fleet et al. (1996); [12] Crocket et al. (1997); [13] Peach and Mathez (1996); [14] Righter et al. (2004); [15] Brenan et al. (2003); [16] Brenan et al. (2005); [17] Hill et al. (2000); [18] Fonseca et al. (2007); [19] Sharp et al. (2014); [20] Brenan et al. (2012).

[a]Indicates values for Re from reference 6, and an oxygen fugacity of FMQ-3.

D (garnet/melt) is only available for Re, for which a value of 1 is used based on studies of 6 and 7; for all other HSEs *D* (garnet/melt) = 0.05 is used.

Bolded values are those used in modeling in Figs. 11 and 12. The sulfide/melt values chosen reflect the fact that *D*(Pd) and *D*(Ir) have similar values and sulfide should not fractionate these two elements (Peach et al. 1994).

simply be sulfide undersaturated at low pressure. Regardless of the cause of low (1600 ppm) S contents, S will increase during silicate (or oxide) fractionation in a closed system until sulfide saturates again (Fig. 10B). The importance of this process for HSEs will be highlighted below.

One anomaly among this group of samples deserves discussion: Dhofar 019, whose measured S content is 4500 ppm (Taylor et al. 2002). The high S contents in Dho 019 could be due to desert weathering, in which the bulk S is in the form of sulfate. A second analysis of Dho 019 by Franz et al. (2014) shows a lower S content (1700 ppm) and evidence that the sulfur is indeed in the form of sulfide. This concentration is consistent with the levels measured in other olivine-phyric shergottites and therefore this second analysis is considered more reliable and unaffected by weathering. Implications of sulfide saturation and undersaturation for HSE contents during fractionation will be discussed in the Fractional Crystallization section below.

Mantle Melting

The Dreibus and Wänke Martian mantle composition is consistent with many fundamental geophysical and geochemical constraints we have for the Martian mantle, and thus is adopted here for detailed modeling of mantle melting (Longhi et al. 1992). Melting experiments on this bulk composition (Matsukage et al. 2013) between 1.0 and 4.5 GPa yield major element (MgO and FeO) contents of melts and the mineralogy of the residual mantle (oliv, opx, cpx, sp, gt), both of which can be used to constrain the HSE contents of the mantle melts. Using a batch melting model, the results of the experiments by Matsukage et al. (2013), and published *D*(HSE) mineral/melt (Table 5), we have calculated HSE contents of mantle melts at variable degrees of melting at several different pressures (Fig. 11). These HSE contents can then be compared to the range measured for shergottites (Fig. 11), and illustrates that many shergottites could represent melts of the Dreibus and Wänke mantle composition produced between 1 and 4 GPa. Thus, some of the variation observed among Martian meteorite HSE contents can be attributed to polybaric melting processes, but we will show in the next section that fractional crystallization at sulfide-saturated and -undersaturated conditions will produce an even larger range of HSE contents.

Fractional Crystallization

Identification of Primitive Melts

Primitive mantle melts can be difficult to unequivocally identify (e.g., Asimow and Longhi 2004), but several lines of evidence can be examined, and garner strength from comparisons to terrestrial basalt–

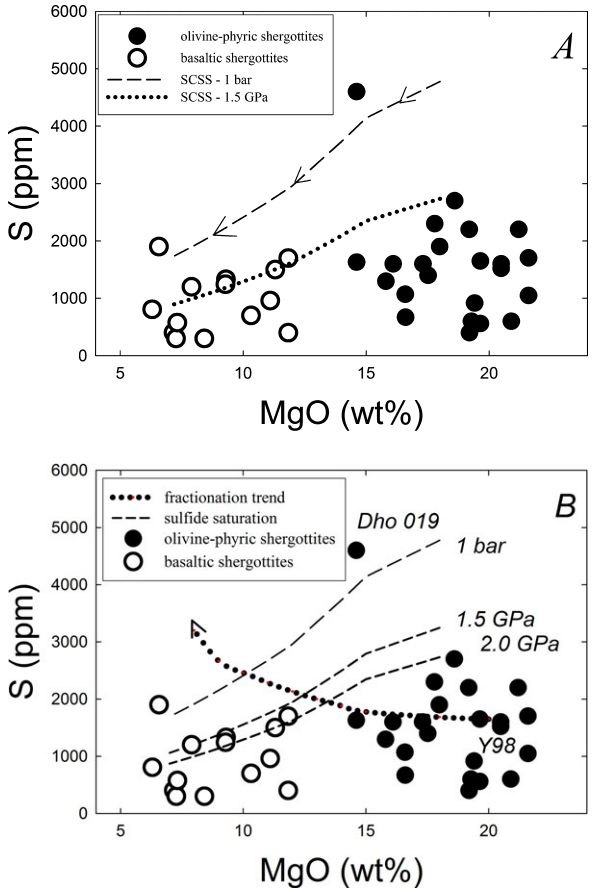

Fig. 10. Calculated S contents at saturation for a liquid line of descent of shergottitic liquids (after Symes et al. 2008; Rapp et al. 2013), along with S and MgO contents measured in shergottites (from Franz et al. [2014]; Yang et al. [2014]; Lodders [1998]; Dreibus et al. [2000]; Shirai and Ebihara [2004]; Sarbadhikari et al. [2009]; Zipfel et al. [2000]; Anand et al. [2008] and sources in Table 5). A) SCSS for a liquid line of descent at 1 bar and 1.5 GPa. Many olivine-phyric shergottites contain S contents consistent with sulfide saturation at high pressures. B) The same SCSS curves (plus one more at 2.0 GPa) and data along with a heavy dashed line that indicates the path of a sulfide-undersaturated olivine-phyric shergottite liquid that become S-enriched during fractionation, and crosses the SCSS lines as it becomes more evolved. In this way, an originally sulfide-undersaturated melt can become sulfide saturated late in a fractionation series like many basaltic shergottites.

mantle relations. Identification of primary terrestrial basalts is commonly done using trends of MgO and compatible trace elements such as Ni or Cr (e.g., Sato 1977). Experimental studies can be used to test whether certain bulk compositions can be primary, or instead reflect crystal accumulation. For example, multiple saturation experiments on various olivine-phyric shergottite compositions have led to the conclusion that several can represent primitive Martian melts—Yamato-980459, NWA 1068, NWA 5789, and NWA 6234 (Musselwhite et al. 2006; Filiberto et al. 2010, 2012). Melts of these compositions could be considered parental to more evolved melts derived by fractional crystallization.

Sulfide Saturation

Consideration of the presence of sulfide in the Martian mantle, and if the resulting melts were saturated or undersaturated in sulfide, is rarely made when assessing the evolution of shergottite HSE abundances. Lorand et al. (2005) demonstrate that sulfide and magnetite saturate late in the fractionation series for Martian magmas, and this is very important with respect to the HSE. Bulk S contents indicate that olivine-phyric shergottites may be S-saturated at depth and become S-undersaturated when they ascend to the surface. Using HSE partition coefficient data and the two scenarios where shergottites are sulfide undersaturated or sulfide saturated, it is possible to calculate the liquid lines of descent for these Martian basaltic magmas, to test if measured HSE contents are consistent with calculated concentrations. As before, we use the results of MELTS calculations of a primitive shergottite to a more evolved basaltic shergottite (after Symes et al. [2008] and Rapp et al. [2013]) for representation of fractional crystallization.

The first modeling scenario is the case where primitive shergottites are sulfide undersaturated, and contain 1600 ppm S. During fractionation of this melt, the S contents are driven up while the MgO contents decrease due to fractionation of olivine, pyroxene, and spinel. Eventually, the S contents become high enough to cross into the sulfide saturation field, and it is here that sulfide becomes a major fractionating phase for the HSE. This late sulfide (and magnetite) fractionation was also predicted by Lorand et al. (2005). In this case, the compatible HSEs such as Ir and Os decrease slightly during the initial sulfide-undersaturated stage of the olivine and chromite fractionation, and then decrease substantially after the stability of sulfide occurs (Fig. 12). For incompatible HSEs, such as Pd and Pt, concentrations increase during the initial stage of sulfide-undersaturated olivine and chromite fractionation, but then also decrease in the later stages where sulfide becomes stable. This scenario can explain many of the data for both primitive olivine-phyric and evolved basaltic shergottites (Fig. 12).

A second scenario is required to explain several additional samples. If a primitive magma is sulfide saturated (requiring near 4000 ppm S at 1 bar, or approximately 1600 ppm at 1.5 GPa), its HSE contents will be extremely low compared to other undersaturated shergottites due to the strong effect of residual sulfide in the source. Differences in HSE contents between

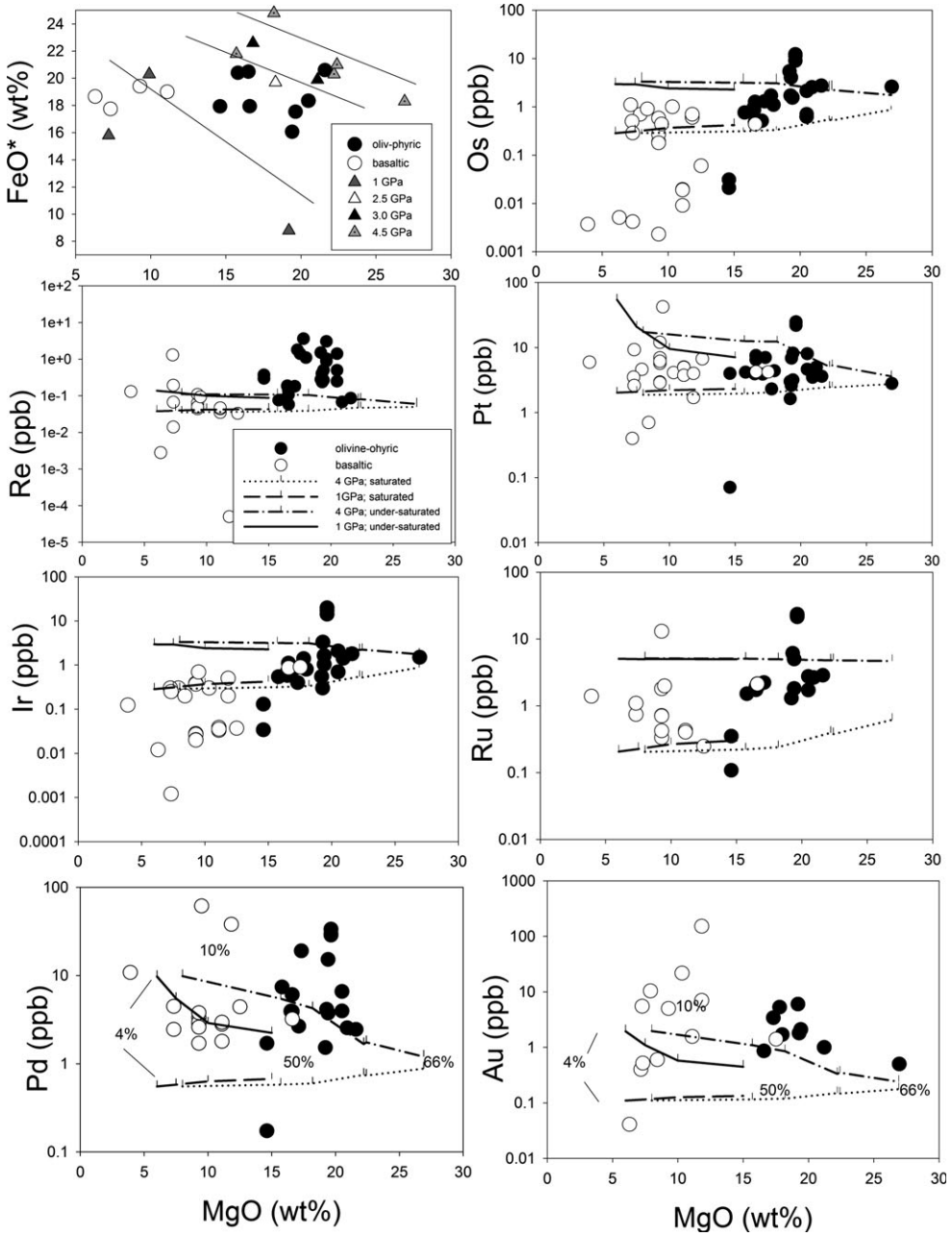

Fig. 11. Variation of FeO–MgO and HSE–MgO contents of Martian mantle melts, as derived from the experiments of Matsukage et al. (2013). Melts at four different pressures are plotted for comparison to FeO, MgO, and HSE contents of shergottites (samples and sources the same as in Figs. 1 and 6). HSE contents for mantle melts are calculated using the results of Matsukage et al.'s (2013) experiments, partition coefficients (mineral/melt) for HSE (Table 5), and a batch melting model. Tick marks indicate melt fractions from the experimental results; for clarity, only the melt fraction values for the high and low ends of melting are shown as % values for the 1 GPa and 4.5 GPa trends.

primitive undersaturated and saturated melts are obvious (Fig. 12), and we describe three cases. First, of the primitive shergottites we have in collections, Dhofar 019, Sau005, EET 79001 lithology A, DaG 476, and NWA 5789 all have low HSE concentrations; these may have been sulfide-saturated melts. Second, the basaltic shergottites QUE 94201 and EET A79001 lithology B have low HSE contents that have been difficult to explain (e.g., Jones et al. 2003). In this case, however, the low contents can be explained by fractionation of a sulfide-saturated parental liquid that starts out with a very low HSE concentration. If such a parent was

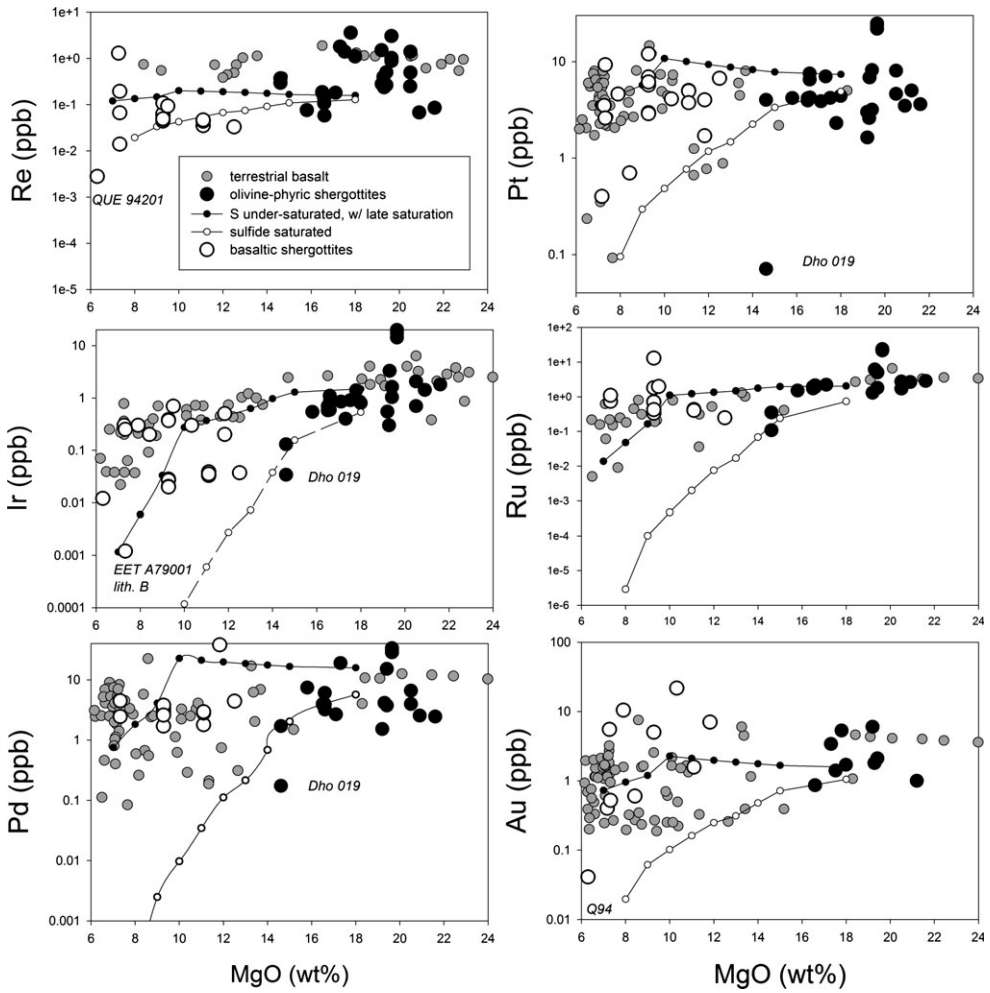

Fig. 12. HSE–MgO diagrams for shergottites, compared to two fractionation trends discussed in text—sulfide saturated and sulfide undersaturated. Variation of the HSEs Re, Pt, Ir, Ru, Au, and Pd in olivine-phyric and basaltic shergottites can largely be explained by both sulfide saturated and undersaturated fractionation trends. In general, Au, Pd, and Pt are incompatible, whereas Ir, Ru, and Re are compatible. The small solid circles indicate calculated fractional crystallization trends using the partition coefficients in Table 5, and assuming sulfide undersaturation until the very late stages of crystallization where sulfide becomes stable. The small open circles indicate calculated fractional crystallization trends using the partition coefficients in Table 5, and assuming sulfide saturation throughout the crystallization. These two endmember examples encompass most of the HSE variation; in particular, the saturated trend helps to explain a few shergottites that have very low HSE concentrations (EET A79001 lithology B, QUE 94201 [Q94 in Au panel], and Dho 019, although the latter may also be due to extreme desert weathering). Data sources for terrestrial samples and shergottites are the same as in Figs. 1 and 6.

sulfide saturated, and rose to the surface (and therefore became undersaturated), with some additional fractionation it would become saturated again, causing even further lowering of the HSE contents. Third, ALH 84001 has low HSE contents and, again, this concept helps us to understand the possibility that the parental magma of orthopyroxenite ALH 84001 may have been sulfide saturated, thus leaving very little HSE to enter the cumulate phases in this rock (mainly orthopyroxene). This had been suggested by Jones et al. (2003), and recent work by Barrat and Bollinger (2010) shows that the parental liquid to ALH 84001 could indeed have been a basaltic shergottite. Our assessment here supports this notion, and is also consistent with the fact that several of the evolved shergottites are sulfide saturated. A parental liquid giving rise to an orthopyroxenite is also likely to be an evolved SiO_2-saturated liquid like these other evolved samples. Thus, QUE 94201, EET A79001 lithology B, and the parental melt to ALH 84001 could have very low HSE contents due to both early and late sulfide saturation (Fig. 12).

Defining the role of magmatic sulfide in shergottite magmatism has been critically important to understanding the distribution of HSEs. The fact that some shergottites are sulfide saturated and some are not shows some analogous behavior to what is observed

with terrestrial magmas in that komatiites are sulfide undersaturated and MORB and other basaltic magmas are sulfide saturated (e.g., Holzheid and Grove 2002). Although olivine is clearly an important phase for some elements compatible in its structure (e.g., Or, Ir, Re), all phases—sulfide, olivine, and spinels such as chromite and magnetite—must be considered for a comprehensive understanding of HSEs in Martian samples. The possibility of incongruent melting of sulfides to form a solid pyrrhotite-like residue that retains the IPGE (Ir, Os, Ru) while releasing the PPGE (Pt, Pd, Rh) should not be dismissed (e.g., Luguet et al. 2004; Bézos et al. 2005), but it is not necessary to call on this mechanism to explain the range of HSE contents observed among the shergottites.

Combined Causes of Dispersion of HSE Concentrations in Martian Meteorites

The wide range of HSE contents observed among Martian meteorites can be explained by a combination of sulfide saturation or undersaturation in primitive shergottites, mantle melting, and subsequent magmatic fractionation involving chromite, olivine, pyroxene, and magmatic sulfide. Olivine-phyric shergottites contain S contents that are consistent with sulfide saturation at high pressures, but could also have formed sulfide undersaturated at lower pressures. As a result, HSE contents in olivine-phyric shergottites can span a range of concentrations depending on the state of sulfide saturation or undersaturation. The basaltic shergottites, which are more evolved and may represent fractionated liquids from more primitive olivine-rich shergottites, have S contents that are as high as, if not higher than, the primitive shergottites. In many cases (e.g., EET A79001 lithology B, Zagami, Shergotty), the S contents are high enough to be considered sulfide-saturated values (Fig. 10), and indicate that the basaltic shergottites may have become sulfide saturated during their fractionation to more evolved liquids. These observations for HSEs in the basaltic shergottites show that HSE contents can be significantly changed in melts depending on whether a basalt is S-saturated or undersaturated. Overlap of Martian melts with terrestrial mantle and melt samples on an HSE-MgO diagram is not complete for every HSE (e.g., Au, Pd, Re, Pt), and is apparently coincidental due to the role of these three processes, as well as the fact that the HSE contents are plotted on a log scale, which reduces the appearance of the otherwise large range of HSE contents at any given MgO content. Any detailed comparison of Martian melts to terrestrial mantle and melts on diagrams like Fig. 1 will be misleading without a detailed consideration of melting, fractionation, and sulfide saturation processes.

CONCLUSIONS

Calculated mantle HSE contents, resulting from metal–silicate equilibrium at moderate depth in the Martian interior, fall within the range of HSE contents of primitive Martian meteorites. This approach predicts a primitive mantle with subchondritic Re/Os and superchondritic Pt/Ir and Pd/Ir ratios. This indicates that core formation alone could have set the HSE contents of the Martian mantle, thus obviating the need for late chondritic additions or a late veneer. It also indicates that broad classes of siderophile elements in the Martian mantle are consistent with an intermediate depth magma ocean in early Mars—including volatile and moderately, slightly, and highly siderophile elements (Righter and Chabot 2011; Yang et al. 2014; this study). These constraints will ultimately be useful in deciphering the detailed chronology of early Mars and determining if it occurred quickly with protoplanets still differentiating and in the presence of nebular gas (Dauphas and Pourmand 2011; Kobayashi and Dauphas 2013), or if it required a longer accretion time scale and possible need for giant impacts (Sasaki and Abe 2007; Morishima et al. 2013).

Acknowledgments—We would like to dedicate this paper to Mike Drake who, along with Chris Capobianco, recognized the need for HSE partitioning data to help interpret terrestrial and planetary HSE data; a challenging endeavor at the relatively flexible conditions of the one bar gas mixing furnace, but an even thornier one at the inflexible high pressure conditions available in the solid media apparatus. This research is supported by NASA RTOPs to KR from the NASA Mars Fundamental Research and Cosmochemistry programs. Research performed at FSU was supported by grants from the NASA Cosmochemistry program to MH. The ASU SIMS facility is supported by NSF EAR 0960334. Discussions with and comments of J. Jones, A. Brandon, T. Lapen, and M. Righter are appreciated. Reviews of a very early version of this paper by J.-P. Lorand, and journal reviews by S. Huang and an anonymous reviewer, are also very much appreciated.

Editorial Handling—Dr. Stein Jacobsen

REFERENCES

Agee C. B., Wilson N. V., McCubbin F. M., Ziegler K., Polyak V. J., Sharp Z. D., Asmerom Y., Nunn M. H., Shaheen R., Thiemens M. H., Steele A., Fogel M. L., Bowden R., Glamoclija M., Zhang Z., and Elardo S. M. 2013. Unique meteorite from Early Amazonian Mars: Water-rich basaltic breccia Northwest Africa 7034. *Science* 339:780–785.

Anand M., James S., Greenwood R. C., Johnson D., Franchi I. A., and Grady M. M. 2008. Mineralogy and geochemistry of shergottite RBT 04262 (abstract #2173). 39th Lunar and Planetary Science Conference. CD-ROM.

Asimow P. D. and Longhi J. 2004. The significance of multiple saturation points in the context of polybaric near-fractional melting. *Journal of Petrology* 45:2349–2367.

Barnes S.-J., Naldrett A. J., and Gorton M. P. 1985. The origin of the fractionation of platinum group elements in terrestrial magmas. *Chemical Geology* 53:303–323.

Barrat J. A. and Bollinger C. 2010. Geochemistry of the Martian meteorite ALH 84001, revisited. *Meteoritics & Planetary Science* 45:495–512.

Barrat J. A., Jambon A., Bohn M., Gillet P., Sautter V., Göpel C., Lesourd M., and Keller F. 2002. Petrology and chemistry of the picritic shergottite Northwest Africa 1068 (NWA 1068). *Geochimica et Cosmochimica Acta* 66:3505–3518.

Becker H., Horan M. F., Walker R. J., Gao S., Lorand J. P., and Rudnick R. L. 2006. Highly siderophile element composition of the Earth's primitive upper mantle: Constraints from new data on peridotite massifs and xenoliths. *Geochimica et Cosmochimica Acta* 70:4528–4550.

Bezmen N. I., Asif M., Brügmann G. E., Romanenko I. M., and Naldrett A. J. 1994. Distribution of Pd, Rh, Ru, Jr, Os, and Au between sulfide and silicate metals. *Geochimica et Cosmochimica Acta* 58:1251–1260.

Bézos A., Lorand J. P., Humler E., and Gros M. 2005. Platinum-group element systematics in mid-oceanic ridge basaltic glasses from the Pacific, Atlantic, and Indian Oceans. *Geochimica et Cosmochimica Acta* 69:2613–2627.

Borisov A. and Palme H. 1996. Experimental determination of the solubility of Au in silicate melts. *Mineralogy and Petrology* 56:297–312.

Borisov A. and Palme H. 1997. Experimental determination of the solubility of platinum in silicate melts. *Geochimica et Cosmochimica Acta* 61:4349–4357.

Borisov A., Palme H., and Spettel B. 1994. Solubility of palladium in silicate melts: Implications for core formation in the Earth. *Geochimica et Cosmochimica Acta* 58:705–716.

Bottke W. F., Walker R. J., Day J. M., Nesvorny D., and Elkins-Tanton L. 2010. Stochastic late accretion to Earth, the Moon, and Mars. *Science* 330:1527–1530.

Brandon A. D., Walker R. J., Morgan J. W., and Goles G. G. 2000. Re-Os isotopic evidence for early differentiation of the Martian mantle. *Geochimica et Cosmochimica Acta* 64:4083–4095.

Brandon A. D., Puchtel I. S., Walker R. J., Day J., Irving A. J., and Taylor L. A. 2012. Evolution of the Martian mantle inferred from the ^{187}Re–^{187}Os isotope and highly siderophile element abundance systematics of shergottite meteorites. *Geochimica et Cosmochimica Acta* 76:206–235.

Brenan J. M. and McDonough W. F. 2009. Core formation and metal-silicate fractionation of osmium and iridium from gold. *Nature Geosciences* 2:798–801.

Brenan J. M., McDonough W. F., and Dalpe C. 2003. Experimental constraints on the partitioning of rhenium and some platinum group elements between olivine and silicate melt. *Earth and Planetary Science Letters* 212:135–150.

Brenan J. M., McDonough W. F., and Ash R. 2005. An experimental study of the solubility and partitioning of iridium, osmium and gold between olivine and silicate melt. *Earth and Planetary Science Letters* 237:855–872.

Brenan J. M., Finnigan C. F., McDonough W. F., and Homolova V. 2012. Experimental constraints on the partitioning of Ru, Rh, Ir, Pt and Pd between chromite and silicate melt: The importance of ferric iron. *Chemical Geology* 302:16–32.

Brügmann G. E., Arndt N. T., Hofmann A. W., and Tobschall H. J. 1987. Noble metal abundances in komatiite suites from Alexo, Ontario and Gorgona Island, Colombia. *Geochimica et Cosmochimica Acta* 51:2159–2169.

Burgess R., Wright I. P., and Pillinger C. T. 1989. Distribution of sulphides and oxidized sulphur components in SNC meteorites. *Earth and Planetary Science Letters* 93:314–320.

Burghele A., Dreibus G., Palme H., Rammensee W., Spettel B., Weckwerth G., and Wänke H. 1983. Chemistry of shergottites and the shergottite parent body (SPB): Further evidence for the two component model for planet formation (abstract). 14th Lunar and Planetary Science Conference. p. 80.

Burns R. G. 1987. Ferric sulfates on Mars. *Journal of Geophysical Research* 92:570–575.

Capobianco C. J. and Drake M. J. 1990. Partitioning of ruthenium, rhodium, and palladium between spinel and silicate melt and implications for platinum group element fractionation trends. *Geochimica et Cosmochimica Acta* 54:869–874.

Capobianco C. J., Drake M. J., and Rogers P. S. Z. 1991. Crystal/melt partitioning of Ru, Rh, and Pd for silicate and oxide basaltic liquidus phases. Proceedings, 22nd Lunar and Planetary Science Conference. pp. 179–180.

Capobianco C. J., Hervig R. L., and Drake M. J. 1994. Experiments on crystal/liquid partitioning of Ru, Rh and Pd for magnetite and hematite solid solutions crystallized from silicate melt. *Chemical Geology* 113:23–43.

Chabot N. L. and Agee C. B. 2003. Core formation in the Earth and Moon: New experimental constraints from V, Cr, and Mn. *Geochimica et Cosmochimica Acta* 67:2077–2091.

Chabot N. L., Campbell A. J., Jones J. H., Humayun M., and Agee C. B. 2003. An experimental test of Henry's Law in solid metal-liquid metal systems with implications for iron meteorites. *Meteoritics & Planetary Science* 38:181–196.

Chou C. L. 1978. Fractionation of siderophile elements in the Earth's upper mantle. Proceedings, 9th Lunar and Planetary Science Conference. pp. 219–230.

Clark B. and Baird A. K. 1979. Is the Martian lithosphere sulfur-rich? *Journal of Geophysical Research* 84:8395–8403.

Cottrell E. and Walker D. 2006. Constraints on core formation from Pt partitioning in mafic silicate liquids at high temperatures. *Geochimica et Cosmochimica Acta* 70:1565–1580.

Crocket J. H., Fleet M. E., and Stone W. E. 1992. Experimental partitioning of osmium, iridium and gold between basalt melt and sulphide liquid at 1300°C. *Australian Journal of Earth Sciences* 39:427–432.

Crocket J. H., Fleet M. E., and Stone W. E. 1997. Implications of composition for experimental partitioning of platinum-group elements and gold between sulfide liquid and basalt melt: The significance of nickel content. *Geochimica et Cosmochimica Acta* 61:4139–4149.

Dale C. W., Burton K. W., Greenwood R. C., Gannoun A., Wade J., Wood B. J., and Pearson D. G. 2012. Late accretion on the earliest planetesimals revealed by the highly siderophile elements. *Science* 336:72–75.

Dasgupta R. and Walker D. 2008. Carbon solubility in core melts in a shallow magma ocean environment and distribution of carbon between the Earth's core and the mantle. *Geochimica et Cosmochimica Acta* 72:4627–4641.

Dauphas N. and Pourmand A. 2011. Hf-W-Th evidence for rapid growth of Mars and its status as a planetary embryo. *Nature* 473:489–492.

Debaille V., Brandon A. D., Yin Q. Z., and Jacobsen B. 2008. Martian mantle mineralogy investigated by the ^{176}Lu-^{176}Hf and ^{147}Sm-^{143}Nd systematics of shergottites. *Earth and Planetary Science Letters* 269:186–199.

Ding S., Dasgupta R., and Tsuno K. 2014. Sulfur concentration of Martian basalts at sulfide saturation at high pressures and temperatures–Implications for deep sulfur cycle on Mars. *Geochimica et Cosmochimica Acta* 131:227–246.

Drake M. J. 1980. Trace elements as quantitative probes of differentiation processes in planetary interiors. *Reviews of Geophysics* 18:11–25.

Dreibus G. and Wänke H. 1985. Mars, a volatile-rich planet. *Meteoritics* 20:367–381.

Dreibus G., Palme H., Rammensee W., Spettel B., Weckwerth G., and Wänke H. 1982. Composition of the Shergotty parent body: Further evidence of a two component model for planet formation (abstract). 13th Lunar and Planetary Science Conference. pp. 186–187.

Dreibus G., Spettel B., Haubold R., Jochum K. P., Palme H., Wolf D., and Zipfel J. 2000. Chemistry of a new shergottite: Sayh al Uhaymir 005 (abstract). *Meteoritics & Planetary Science* 35:A49.

Ertel W., O'Neill H. St. C., Sylvester P. J., Dingwell D. B., and Spettel B. 2001. The solubility of rhenium in silicate melts: Implications for the geochemical properties of rhenium at high temperatures. *Geochimica et Cosmochimica Acta* 65:2161–2170.

Ertel W., Walter M. J., Drake M. J., and Sylvester P. J. 2006. Experimental study of platinum solubility in silicate melt to 14 GPa and 2273K: Implications for accretion and core formation in Earth. *Geochimica et Cosmochimica Acta* 70:2591–2602.

Filiberto J., Treiman A. H., and Le L. 2008. Crystallization experiments on a Gusev Adirondack basalt composition. *Meteoritics & Planetary Science* 43:1137–1146.

Filiberto J., Musselwhite D. S., Gross J., Burgess K., Le L., and Treiman A. H. 2010. Experimental petrology, crystallization history, and parental magma characteristics of olivine-phyric shergottite NWA 1068: Implications for the petrogenesis of "enriched" olivine-phyric shergottites. *Meteoritics & Planetary Science* 45:1258–1270.

Filiberto J., Chin E., Day J., Franchi I. A., Greenwood R. C., Gross J., and Treiman A. H. 2012. Geochemistry of intermediate olivine-phyric shergottite Northwest Africa 6234, with similarities to basaltic shergottite Northwest Africa 480 and olivine-phyric shergottite Northwest Africa 2990. *Meteoritics & Planetary Science* 47:1256–1273.

Fleet M. E., Stone W. E., and Crocket J. H. 1991. Partitioning of palladium, iridium, and platinum between sulfide liquid and basalt melt: Effects of melt composition, concentration, and oxygen fugacity. *Geochimica et Cosmochimica Acta* 55:2545–2554.

Fleet M. E., Crocket J. H., and Stone W. E. 1996. Partitioning of platinum-group elements (Os, Ir, Ru, Pt, Pd) and gold between sulfide liquid and basalt melt. *Geochimica et Cosmochimica Acta* 60:2397–2412.

Fonseca R. O., Mallmann G., O'Neill H. St. C., and Campbell I. H. 2007. How chalcophile is rhenium? An experimental study of the solubility of Re in sulphide mattes. *Earth and Planetary Science Letters* 260:537–548.

Fortenfant S. S., Günther D., Dingwell D. B., and Rubie D. C. 2003. Temperature dependence of Pt and Rh solubilities in a haplobasaltic melt. *Geochimica et Cosmochimica Acta* 67:123–131.

Franz H. B., Kim S. T., Farquhar J., Day J. M., Economos R. C., McKeegan K. D., and Dottin J. III. 2014. Isotopic links between atmospheric chemistry and the deep sulphur cycle on Mars. *Nature* 508:364–368.

Gaboardi M. and Humayun M. 2009. Elemental fractionation during LA-ICP-MS analysis of silicate glasses: Implications for matrix-independent standardization. *Journal of Analytical Atomic Spectrometry* 24:1188–1197.

Ghiorso M. and Sack R. O. 1995. Chemical mass transfer in magmatic processes IV. A revised and internally consistent thermodynamic model for the interpolation and extrapolation of liquid-solid equilibria in magmatic systems at elevated temperatures and pressures. *Contributions Mineralogy Petrology* 119:197–212.

Gueddari K., Piboule M., and Amossé J. 1996. Differentiation of platinum-group elements (PGE) and of gold during partial melting of peridotites in the lherzolitic massifs of the Betico-Rifean range (Ronda and Beni Bousera). *Chemical Geology* 134:181–197.

Handler M. R. and Bennett V. C. 1999. Behaviour of platinum-group elements in the subcontinental mantle of eastern Australia during variable metasomatism and melt depletion. *Geochimica et Cosmochimica Acta* 63:3597–3618.

Herd C. D. 2008. Basalts as probes of planetary interior redox state. *Reviews in Mineralogy and Geochemistry* 68:527–553.

Hernlund J., Leinenweber K., Locke D., and Tyburczy J. A. 2006. A numerical model for steady-state temperature distributions in solid-medium high-pressure cell assemblies. *American Mineralogist* 91:295–305.

Hervig R. L., Mazdab F. K., Danielson L., Sharp T. G., Hamed A., and Williams P. 2004. SIMS microanalyses for Au in silicates. *American Mineralogist* 89:498–504.

Hill E., Wood B. J., and Blundy J. D. 2000. The effect of Ca-Tschermaks component on trace element partitioning between clinopyroxene and silicate melt. *Lithos* 53:203–217.

Holzheid A. and Grove T. L. 2002. Sulfide saturation limits in silicate melts and their implications to core formation scenarios for terrestrial planets. *American Mineralogist* 87:227–237.

Holzheid A., Sylvester P., O'Neill H. S. C., Rubie D. C., and Palme H. 2000. Evidence for a late chondritic veneer in the Earth's mantle from high-pressure partitioning of palladium and platinum. *Nature* 406:396–399.

Humayun M. 2012. Chondrule cooling rates inferred from diffusive profiles in metal lumps from the Acfer 097 CR2 chondrite. *Meteoritics & Planetary Science* 47:1191–1208.

Humayun M., Simon S. B., and Grossman L. 2007. Tungsten and hafnium distribution in calcium-aluminum inclusions (CAIs) from Allende and Efremovka. *Geochimica et Cosmochimica Acta* 71:4609–4627.

Humayun M., Nemchin A., Zanda B., Hewins R. H., Grange M., Kennedy A., Lorand J.-P., Göpel C., Fieni C., Pont S., and Deldicque D. 2013. Origin and age of the earliest Martian crust from meteorite NWA 7533. *Nature* 503:513–516.

Jagoutz E., Palme H., Baddenhausen H., Blum K., Cendales M., Dreibus G., and Lorenz V. 1979. The abundances of major, minor and trace elements in the earth's mantle as derived from primitive ultramafic nodules. Proceedings, 10th Lunar and Planetary Science Conference. pp. 2031–2050.

Jochum K. P., Weis U., Stoll B., Kuzmin D., Yang Q., Raczek I., and Enzweiler J. 2011. Determination of reference values for NIST SRM 610–617 glasses following ISO guidelines. *Geostandards and Geoanalytical Research* 35:397–429.

Jones J. H. and Drake M. J. 1986. Geochemical constraints on core formation in the Earth. *Nature* 322:221–228.

Jones J. H., Neal C. R., and Ely J. C. 2003. Signatures of the highly siderophile elements in the SNC meteorites and Mars: A review and petrologic synthesis. *Chemical Geology* 196:21–41.

Karner J. M., Papike J. J., Shearer C. K., McKay G., Le L., and Burger P. 2007. Valence state partitioning of Cr and V between pyroxene-melt: Estimates of oxygen fugacity for Martian basalt QUE 94201. *American Mineralogist* 92:1238–1241.

Kiefer W. S. 2003. Melt in the Martian mantle: Shergottite formation and implications for present-day mantle convection on Mars. *Meteoritics & Planetary Science* 38:1815–1832.

Kimura K., Lewis R. S., and Anders E. 1974. Distribution of gold and rhenium between nickel-iron and silicate melts: Implications for the abundance of siderophile elements on the Earth and Moon. *Geochimica et Cosmochimica Acta* 38:683–701.

Kobayashi H. and Dauphas N. 2013. Small planetesimals in a massive disk formed Mars. *Icarus* 225:122–130.

Kong P., Ebihara M., and Palme H. 1999. Siderophile elements in Martian meteorites and implications for core formation in Mars. *Geochimica et Cosmochimica Acta* 63:1865–1875.

Lapen T. J., Righter M., Brandon A. D., Debaille V., Beard B. L., Shafer J. T., and Peslier A. H. 2010. A younger age for ALH 84001 and its geochemical link to shergottite sources in Mars. *Science* 328:347–351.

Laurenz V., Fonseca R. O. C., Ballhaus C., and Sylvester P. J. 2010. Solubility of palladium in picritic melts: 1. The effect of iron. *Geochimica et Cosmochimica Acta* 74:2989–2998.

Laurenz V., Rubie D. C., and Frost D. J. 2014. Metal-silicate partitioning of highly siderophile elements in S-bearing systems—Implications for the formation of Earth's core. V.M. Goldschmidt meeting, Sacramento, CA, 1368.

Lewis R. D., Lofgren G. E., Franzen H. F., and Windom K. E. 1993. The effect of Na vapor on the Na content of chondrules. *Meteoritics* 28:622–628.

Lindstrom D. J. and Jones J. H. 1996. Neutron activation analysis of multiple 10–100 μg glass samples from siderophile element partitioning experiments. *Geochimica et Cosmochimica Acta* 60:1195–1203.

Liu Y., Ge Y., and Yu D. 2009. Thermodynamic descriptions for Au–Fe and Na–Zn binary systems. *Journal of Alloys and Compounds* 476:79–83.

Lodders K. 1998. A survey of shergottite, nakhlite and chassigny meteorites whole-rock compositions. *Meteoritics & Planetary Science* 33:A183–A190.

Lodders J. and Fegley B. Jr. 1997. An oxygen isotope model for the composition of Mars. *Icarus* 126:373–394.

Longhi J., Knittle E., Holloway J. R., Wanke H. 1992. The bulk composition, mineralogy and internal structure of Mars. In *Mars*, edited by Kieffer H. H., Jakosky B. M., Snyder C. W., and Matthews M. S. Tucson, Arizona: The University of Arizona Press. pp. 184–208.

Lorand J. P., Pattou L., and Gros M. 1999. Fractionation of platinum-group elements and gold in the upper mantle: A detailed study in Pyrenean orogenic lherzolites. *Journal of Petrology* 40:957–981.

Lorand J. P., Schmidt G., Palme H., and Kratz K. L. 2000. Highly siderophile element geochemistry of the Earth's mantle: New data for the Lanzo (Italy) and Ronda (Spain) orogenic peridotite bodies. *Lithos* 53:149–164.

Lorand J. P., Chevrier V., and Sautter V. 2005. Sulfide mineralogy and redox conditions in some shergottites. *Meteoritics & Planetary Science* 40:1257–1272.

Luguet A., Lorand J. P., Alard O., and Cottin J. Y. 2004. A multi-technique study of platinum group element systematic in some Ligurian ophiolitic peridotites, Italy. *Chemical Geology* 208:175–194.

Ma M.-S., Laul J. C., Smith M. R., and Schmitt R. A. 1982. Chemistry of shergottites Elephant Moraine A79001 and Zagami (abstract). 12th Lunar and Planetary Science Confernce. p. 451.

Mallmann G. and O'Neill H. St. C. 2007. The effect of oxygen fugacity on the partitioning of Re between crystals and silicate melt during mantle melting. *Geochimica et Cosmochimica Acta* 71:2837–2857.

Malvin D. J., Drake M. J., Benjamin T. M., Duffy C. J., Hollander M., and Rogers P. S. 1986. Experimental partitioning studies of siderophile elements amongst lithophile phases: Preliminary results using PIXE microprobe analysis. Proceedings, 18th Lunar and Planetary Science Conference. pp. 514–515.

Mann U., Frost D. J., Rubie D. C., Becker H., and Audétat A. 2012. Partitioning of Ru, Rh, Pd, Re, Ir and Pt between liquid metal and silicate at high pressures and high temperatures—Implications for the origin of highly siderophile element concentrations in the Earth's mantle. *Geochimica et Cosmochimica Acta* 84:593–613.

Matsukage K. N., Nagayo Y., Whitaker M. L., Takahashi E., and Kawasaki T. 2013. Melting of the Martian mantle from 1.0 to 4.5 GPa. *Journal of Mineralogical and Petrological Sciences* 108:201–214.

McSween H. Y. and Jarosewich E. 1983. Petrogenesis of the EET A79001 meteorite: Multiple magma pulses on the shergottite parent body. *Geochimica et Cosmochimica Acta* 47:1501–1513.

Meisel T., Walker R. J., Irving A. J., and Lorand J. P. 2001. Osmium isotopic compositions of mantle xenoliths: A global perspective. *Geochimica et Cosmochimica Acta* 65:1311–1323.

Mezger K., Debaille V., and Kleine T. 2013. Core formation and mantle differentiation on Mars. *Space Science Reviews* 174:27–48.

Mills K. C. 1993. The influence of structure on the physico-chemical properties of Slags. *ISIJ International* 33:148–155.

Mitchell R. H. and Keays R. R. 1981. Abundance and distribution of gold, palladium and iridium in some spinel and garnet lherzolites: Implications for the nature and origin of precious metal-rich intergranular components in the upper mantle. *Geochimica et Cosmochimica Acta* 45:2425–2442.

Morgan J. W. 1986. Ultramafic xenoliths: Clues to Earth's late accretionary history. *Journal of Geophysical Research* 91:12,375–12,387.

Morgan J. W. and Baedecker P. 1983. Elemental composition of sulfide particles from an ultramafic xenolith and the siderophile element content of the upper mantle. Proceedings, 14th Lunar and Planetary Science Conference. pp. 513–514.

Morgan J. W., Wandless G. A., Petrie R. K., and Irving A. J. 1981. Composition of the Earth's upper mantle—I. Siderophile trace elements in ultramafic nodules. *Tectonophysics* 75:47–67.

Morishima R., Golabek G. J., and Samuel H. 2013. N-body simulations of oligarchic growth of Mars: Implications for Hf–W chronology. *Earth and Planetary Science Letters* 366:6–16.

Musselwhite D. S., Dalton H. A., Kiefer W. S., and Treiman A. H. 2006. Experimental petrology of the basaltic shergottite Yamato-980459: Implications for the thermal structure of the Martian mantle. *Meteoritics & Planetary Science* 41:1271–1290.

Mysen B. O. 1991. Relations between structure, redox equilibria of iron, and properties of magmatic liquids. In *Physical chemistry of magmas*, edited by Perchuk L. L. and Kushiro I. New York: Cambridge University Press. pp. 41–98.

Neal C. R., Taylor L. A., Ely J. C., Jain J. C., and Nazarov M. A. 2001. Detailed geochemistry of new shergottite, Dhofar 019 (abstract #1671). 32nd Lunar and Planetary Science Conference. CD-ROM.

Newsom H. E. 1984. The lunar core and the origin of the Moon. *Eos, Transactions American Geophysical Union* 65:369–370.

Newsom H. E. 1995. *Global earth physics: A handbook of physical constants*, AGU Ref. Shelf, vol. 1. Washington, D.C.: American Geophysical Union. pp. 159–189.

Peach C. L. and Mathez E. A. 1996. Constraints on the formation of platinum-group element deposits in igneous rocks. *Economic Geology* 91:439–450.

Peach C. L., Mathez E. A., and Keays R. R. 1990. Sulfide melt-silicate melt distribution coefficients for noble metals and other chalcophile elements as deduced from MORB: Implications for partial melting. *Geochimica et Cosmochimica Acta* 54:3379–3389.

Peach C. L., Mathez E. A., Keays R. R., and Reeves S. J. 1994. Experimentally determined sulfide-melt silicate melt partition coefficients for iridium and palladium. *Chemical Geology* 117:361–377.

Poirier J. P. 1994. Light elements in the Earth's outer core: A critical review. *Physics of the Earth and Planetary Interiors* 85:319–337.

Pouchou J. L. and Pichoir F. 1991. In *Electron probe quantitation*, edited by Heinrich K. F. J. and Newbury D. E. New York: Plenum Press. pp. 31–75.

Puchtel I. S. and Humayun M. 2000. Platinum group elements in Kostomuksha komatiites and basalts: Implications for oceanic crust recycling and core-mantle interaction. *Geochimica et Cosmochimica Acta* 64:4227–4242.

Puchtel I. S. and Humayun M. 2005. Highly siderophile element geochemistry of ^{187}Os-enriched 2.8 Ga Kostomuksha komatiites, Baltic Shield. *Geochimica et Cosmochimica Acta* 69:1607–1618.

Puchtel I. S., Humayun M., Campbell A. J., Sproule R. A., and Lesher C. M. 2004. Platinum group element geochemistry of komatiites from the Alexo and Pyke Hill areas, Ontario, Canada. *Geochimica et Cosmochimica Acta* 68:1361–1383.

Puchtel I. S., Walker R. J., Brandon A. D., and Irving A. J. 2008. Highly siderophile element abundances in SNC meteorites: An update (abstract #1650). 39th Lunar and Planetary Science Conference. CD-ROM.

Puchtel I. S., Walker R. J., Anhaeusser C. R., and Gruau G. 2009. Re–Os isotope systematics and HSE abundances of the 3.5 Ga Schapenburg komatiites, South Africa: Hydrous melting or prolonged survival of primordial heterogeneities in the mantle? *Chemical Geology* 262:355–369.

Rai N. and Van Westrenen W. 2013. Core-mantle differentiation in Mars. *Journal of Geophysical Research: Planets* 118:1195–1203.

Rapp J. F., Draper D. S., and Mercer C. M. 2013. Anhydrous liquid line of descent of Yamato-980459 and evolution of Martian parental magmas. *Meteoritics & Planetary Science* 48:1780–1799.

Reese C. C. and Solomotov V. S. 2006. Fluid dynamics of local Martian magma oceans. *Icarus* 184:102–120.

Rehkämper M., Halliday A. N., Fitton J. G., Lee D. C., Wieneke M., and Arndt N. T. 1999. Ir, Ru, Pt, and Pd in basalts and komatiites: New constraints for the geochemical behavior of the platinum-group elements in the mantle. *Geochimica et Cosmochimica Acta* 63:3915–3934.

Riches A. J., Liu Y., Day J., Puchtel I. S., Rumble D. III, McSween H. Y. Jr., and Taylor L. A. 2011. Petrology and geochemistry of Yamato 984028: A cumulate lherzolitic shergottite with affinities to Y 000027, Y 000047, and Y 000097. *Polar Science* 4:497–514.

Righter K. 2002. Does the Moon have a metallic core? Constraints from giant impact modeling and siderophile elements. *Icarus* 158:1–13.

Righter K. 2011. Prediction of metal–silicate partition coefficients for siderophile elements: An update and assessment of PT conditions for metal–silicate equilibrium during accretion of the Earth. *Earth and Planetary Science Letters* 304:158–167.

Righter K. and Chabot N. L. 2011. Moderately and slightly siderophile element constraints on the depth and extent of melting in early Mars. *Meteoritics & Planetary Science* 46:157–176.

Righter K. and Drake M. J. 1997a. A magma ocean on Vesta: Core formation and petrogenesis of eucrites and diogenites. *Meteoritics & Planetary Science* 32:929–944.

Righter K. and Drake M. J. 1997b. Metal-silicate equilibrium in a homogeneously accreting earth: New results for Re. *Earth and Planetary Science Letters* 146:541–553.

Righter K. and Hauri E. H. 1998. Compatibility of rhenium in garnet during mantle melting and magma genesis. *Science* 280:1737–1741.

Righter K., Drake M. J., and Yaxley G. 1997. Prediction of siderophile element metal-silicate partition coefficients to 20 GPa and 2800°C: The effects of pressure, temperature, oxygen fugacity, and silicate and metallic melt compositions. *Physics of the Earth and Planetary Interiors* 100:115–134.

Righter K., Walker R. J., Warren P. H. 2000. Significance of highly siderophile elements and osmium isotopes in the lunar and terrestrial mantles. In *Origin of the Earth and Moon*, edited by Canup R. M. and Righter K. Tucson, Arizona: The University of Arizona Press. pp. 291–322.

Righter K., Campbell A. J., Humayun M., and Hervig R. L. 2004. Partitioning of Re, Ir, Rh, and Ru between Cr-bearing spinel, olivine, pyroxene and silicate melts. *Geochimica et Cosmochimica Acta* 68:867–880.

Righter K., Humayun M., and Danielson L. 2008a. Partitioning of palladium at high pressures and temperatures during core formation. *Nature Geoscience* 1:321–323.

Righter K., Yang H., Costin G., and Downs R. T. 2008b. Oxygen fugacity in the Martian mantle controlled by carbon: New constraints from the nakhlite MIL 03346. *Meteoritics & Planetary Science* 43:1709–1723.

Righter K., Pando K., and Danielson L. R. 2009a. Experimental evidence for sulfur-rich Martian magmas: Implications for volcanism and surficial sulfur sources. *Earth and Planetary Science Letters* 288:235–243.

Righter M., Lapen T. J., Brandon A. D., Beard B. L., Shafer J. T., and Peslier A. H. 2009b. Lu-Hf Age and isotope systematics of ALH 84001 (abstract #2256). 40th Lunar and Planetary Science Conference. CD-ROM.

Righter K., Pando K. M., Danielson L., and Lee C. T. 2010. Partitioning of Mo, P and other siderophile elements (Cu, Ga, Sn, Ni Co, Cr, Mn, V, and W) between metal and silicate melt as a function of temperature and silicate melt composition. *Earth and Planetary Science Letters* 291:1–9.

Righter K., King C., Danielson L., Pando K., and Lee C. T. 2011. Experimental determination of the metal/silicate partition coefficient of Germanium: Implications for core and mantle differentiation. *Earth and Planetary Science Letters* 304:379–388.

Russell C. T., Raymond C. A., Coradini A., McSween H. Y., Zuber M. T., Nathues A., and Titus T. N. 2012. Dawn at Vesta: Testing the protoplanetary paradigm. *Science* 336:684–686.

Sarbadhikari A. B., Day J., Liu Y., Rumble D. III, and Taylor L. A. 2009. Petrogenesis of olivine-phyric shergottite Larkman Nunatak 06319: Implications for enriched components in Martian basalts. *Geochimica et Cosmochimica Acta* 73:2190–2214.

Sasaki T. and Abe Y. 2007. Rayleigh-Taylor instability after giant impacts: Imperfect equilibration of the Hf-W system and its effect on the core formation age. *Earth, Planets and Space* 59:1035–1045.

Sato H. 1977. Nickel content of basaltic magmas: Identification of primary magmas and a measure of the degree of olivine fractionation. *Lithos* 10:113–120.

Schmidt G., Palme H., Kratz K. L., and Kurat G. 2000. Are highly siderophile elements (PGE, Re and Au) fractionated in the upper mantle of the earth? New results on peridotites from Zabargad. *Chemical Geology* 163:167–188.

Senshu H., Kuramoto K., and Matsui T. 2002. Thermal evolution of a growing Mars. *Journal of Geophysical Research: Planets (1991–2012)*, 107(E12): 1–1.

Sharp M. G., Righter K., and Walker R. J. 2014. Estimation of trace element concentrations of the Lunar Magma Ocean using mineral-melt and metal-silicate partition coefficients. *Meteoritics & Planetary Science*, doi:10.1111/maps.12396.

Shirai N. and Ebihara M. 2004. Chemical characteristics of a Martian meteorite, Yamato 980459. *Antarctic Meteorite Research* 17:55–67.

Shirey S. B. and Walker R. J. 1998. The Re-Os isotope system in cosmochemistry and high-temperature geochemistry. *Annual Review of Earth and Planetary Sciences* 26:423–500.

Smith M. R., Laul J. C., Ma M.-S., Huston T., Verkouteren R. M., Lipschutz M. E., and Schmitt R. A. 1984. Petrogenesis of the SNC (shergottites, nakhlites, chassignites) meteorites: Implications for their origin from a large, dynamic planet, possibly Mars. *Proceedings of the Lunar and Planetary Science Conference 14th; Journal of Geophysical Research* 89(suppl.):B612–B630.

Stone W. E., Crocket J. H., and Fleet M. E. 1990. Partitioning of palladium, iridium, platinum, and gold between sulfide liquid and basalt melt at 1200°C. *Geochimica et Cosmochimica Acta* 54:2341–2344.

Sylvester P. J. and Eggins S. M. 1997. Analysis of Re, Au, Pd, Pt and Rh in NIST glass certified reference materials and natural basalt glasses by laser ablation ICP-MS. *Geostandards Newsletter* 21:215–229.

Symes S. J. K., Borg L. E., Shearer C. K., and Irving A. J. 2008. The age of the Martian meteorite Northwest Africa 1195 and the differentiation history of the shergottites. *Geochimica et Cosmochimica Acta* 72:1696–1710.

Taylor L. A., Nazarov M. A., Shearer C. K., McSween H. Y., Cahill J., Neal C. R., Ivanova M. A., Barsukova L. D., Lentz R. C., Clayton R. N., and Mayeda T. K. 2002. Martian meteorite Dhofar 019: A new shergottite. *Meteoritics & Planetary Science* 37:1107–1128.

Treiman A. H., Jones J. H., and Drake M. J. 1987. Core formation in the shergottite parent body and comparison with the Earth. *Proceedings of the Lunar and Planetary Science Conference, 17th, Part 2, Journal of Geophysical Research* 92:E627–632.

Vogel D. C. and Keays R. R. 1997. The petrogenesis and platinum-group element geochemistry of the Newer Volcanic Province, Victoria, Australia. *Chemical Geology* 136:181–204.

Walker R. J. 2009. Highly siderophile elements in the Earth, Moon and Mars: Update and implications for planetary accretion and differentiation. *Chemie der Erde-Geochemistry* 69:101–125.

Walker R. J., Brandon A. D., Nazarov M. A., Mittlefehldt D., Jagoutz E., and Taylor L. A. 2002. ^{187}Re-^{187}Os isotopic studies of SNC meteorites: An update. 33rd Lunar and Planetary Science Conference. CD-ROM.

Walker R. J., Puchtel I. S., Brandon A. D., and Irving A. J. 2008a. Highly siderophile elements abundances in SNC meteorites: An update. Ground truth from Mars: Science Payoff from a Sample Return Mission, held April 21–23, 2008, Albuquerque, New Mexico. LPI Contribution 1401. pp. 107–108.

Walker R. J., McDonough W. F., Honesto J., Chabot N. L., McCoy T. J., Ash R. D., and Bellucci J. J. 2008b. Modeling fractional crystallization of group IVB iron meteorites. *Geochimica et Cosmochimica Acta* 72:2198–2216.

Walker R. J., Puchtel I. S., Brandon A. D., Day J., and Irving A. J. 2009. ^{187}Re-^{187}Os and highly siderophile element systematics of Shergottites: New puzzles regarding the Martian mantle (abstract #1263). 40th Lunar and Planetary Science Conference. CD-ROM.

Warren P. H. and Kallemeyn G. W. 1996. Siderophile trace elements in ALH84001, other SNC meteorites and eucrites: Evidence of heterogeneity, possibly time-linked, in the mantle of Mars. *Meteoritics & Planetary Science* 31:97–105.

Warren P. H., Kallemeyn G. W., Arai T., and Kaneda K. 1996. Compositional-petrologic investigations of eucrites

and the QUE94201 shergottite (abstract). *Proceedings of the NIPR Symposium on Antarctic Meteorites* 21:195–197.

Warren P. H., Kallemeyn G. W., and Kyte F. T. 1999. Origin of planetary cores: Evidence from highly siderophile elements in Martian meteorites. *Geochimica et Cosmochimica Acta* 63:2105–2122.

Wasson J. T., Ouyang X., Wang J., and Jerde E. 1989. Chemical classification of iron meteorites: XI. Multi-element studies of 38 new irons and the high abundance of ungrouped irons from Antarctica. *Geochimica et Cosmochimica Acta* 53:735–744.

Watson E. B., BenOthman D., Luck J. M., and Hofmann A. W. 1987. Partitioning of U, Pb, Cs, Yb, Hf, Re, and Os between chromian diopside pyroxene and haplobasaltic liquid. *Chemical Geology* 62:191–208.

Watson E., Wark D., Price J., and Van Orman J. 2002. Mapping the thermal structure of solid-media pressure assemblies. *Contributions to Mineralogy and Petrology* 142:640–652.

Wheeler K. T., Walker D., and McDonough W. F. 2011. Pd and Ag metal-silicate partitioning applied to Earth differentiation and core-mantle exchange. *Meteoritics & Planetary Science* 46:199–217.

Yang S., Humayun M., Righter K., Jefferson G., Fields D., and Irving A. J. 2014. Siderophile and chalcophile element abundances in shergottites: Implications for Martian core formation. *Meteoritics & Planetary Science*, doi:10.1111/maps.12384.

Zipfel J., Scherer P., Spettel B., Dreibus G., and Schultz L. 2000. Petrology and chemistry of the new shergottite Dar al Gani 476. *Meteoritics & Planetary Science* 35:95–106.